SPECIAL
OLYMPEX
COLLECTION

Multiscale Interactions Contributing to Enhanced Orographic Precipitation in Landfalling Frontal Systems over the Olympic Peninsula

Brenda Dolan,[a] Steven A. Rutledge,[a] and Kristen L. Rasmussen[a]

[a] Department of Atmospheric Science, Colorado State University, Fort Collins, Colorado

ABSTRACT: Orographic precipitation results from complex interactions between terrain, large-scale flow, turbulent motions, and microphysical processes. This study appeals to polarimetric radar data in conjunction with surface-based disdrometer observations, airborne particle probes, and reanalysis data to study these processes and their interactions as observed during the Olympic Mountain Experiment (OLYMPEX). Radar and disdrometer observations from OLYMPEX, which was conducted over the Olympic Peninsula in the winter of 2015, revealed 3 times as much rain fell over elevated sites compared to those along the ocean and coast. Several events were marked by significant water vapor transport and strong onshore flow. Detailed analysis of four cases demonstrated that the warm sector, which previous authors noted to be a period of strong orographic enhancement over the terrain, is associated not only with deeper warm cloud regions, but also deeper cold cloud regions, with the latter supporting the growth of dendritic ice crystals between 4 and 6 km. This dendritic growth promotes enhanced aggregation just above the melting layer, which then seeds the warm cloud layer below, allowing additional drop growth via coalescence. Periods of subsynoptic variability associated with mesoscale boundaries and low-level jets are shown to locally modify both the ice microphysics as well as surface drop-size distributions. This study explores the spatial and temporal variability of precipitation, cloud microphysics, and their relationship over the complex terrain of the Olympic Peninsula.

SIGNIFICANCE STATEMENT: This study appeals to polarimetric radar, aircraft particle probes, disdrometer data, and reanalysis to investigate the complex interactions between large frontal systems, terrain, and microphysical processes contributing to precipitation characteristics at the surface over the Olympic Peninsula. The study finds that the precipitation is a complex function of the synoptic regime, distance inland, and terrain height. Ice microphysical processes aloft act to modulate the surface rain drop size distributions, and are more important in contributing to higher rain accumulations inland during the later phases of the warm sector, particularly over the middle terrain heights (100–500 m).

KEYWORDS: Complex terrain; Precipitation; Cloud microphysics; Radars/Radar observations

1. Introduction

The Olympic Mountains in western Washington accumulate some of the largest amounts of annual precipitation in the United States, in part due to the prominence of the mountains in close proximity to the ocean, but also due to the location of the storm track bringing frequent extratropical cyclones during the winter months. Under this backdrop, the Olympic Mountains Experiment (OLYMPEX)[1] deployed a large suite of observational platforms, including surface disdrometer networks, ground-based radars, radiosondes, and aircraft, to study precipitation processes and orographic enhancement (Houze et al. 2017).

Previous studies have investigated aspects of the precipitation over this region using OLYMPEX assets. The findings of Zagrodnik et al. (2018) suggest orographic enhancement is characterized by significant quantities of small and moderate drops which are found at middle-elevation sites on windward

[1] OLYMPEX was a National Aeronautics and Space Administration Ground Validation project for the Global Precipitation Measurement (GPM) satellite that took place over the boreal winter of 2015–16.

slopes, and occur typically during the warm sector that has high integrated vapor transport (IVT), strong onshore flow, and elevated freezing levels. Purnell and Kirshbaum (2018) examined the precipitation patterns over the project as a function of the synoptic periods, finding the heaviest precipitation fell during warm front and warm sector periods, supported by seeder–feeder processes. McMurdie et al. (2018) found that reflectivity structures were enhanced over land compared to the ocean within the warm sectors of land falling extratropical cyclones. Zagrodnik et al. (2018) also found perturbations in rain DSDs caused by small-scale subsynoptic features, such as fronts and waves, but more significant DSD differences were noted between frontal regimes. They concluded that the orographic enhancement was largely due to warm rain processes, although ice microphysics were noted to play a role in precipitation development during certain regimes. A modeling study by Zagrodnik et al. (2021) found that uplift over the coastal hills supported enhanced cloud drop self-collection in the warm layer, resulting in high concentrations of small drops that contributed to surface precipitation through fallout. Modeling studies by Conrick and Mass (2019) and Naeger et al. (2020) found that the WRF Model was unable to accurately simulate neither precipitation totals nor drop size distributions. The results of those studies showed the importance of ice processes to rain generation, and that bulk microphysical schemes were not able to fully replicate the contributions from warm rain processes, which they speculated may be related to weaknesses in turbulence parameterizations.

DeLaFrance et al. (2021) investigated the microphysics of enhanced reflectivity and differential reflectivity (Z_{dr}) layers in detail. Aircraft particle probe data in these layers revealed rimed dendrites and irregular particles. These occurred with larger supercooled liquid water contents, which result from strong low-level jet flow directly up the terrain barrier. While these features were observed over both the ocean and the land, they were more pronounced and frequent over land.

These studies demonstrate the multiscale feedbacks between atmospheric stability, turbulence, orographic processes, microphysics and precipitation. Herein, we seek to further our understanding of the precipitation, in-cloud processes, and their complex interactions as a function of space (land versus ocean, distance inland), time (frontal system regime, environment), and terrain height. Specifically, we seek to address the following three science questions: 1) What is the precipitation variability over the OLYMPEX domain as a function of space, time, and terrain height? 2) What is the variability of in-cloud microphysical processes as a function of space and time? 3) How is the observed surface precipitation variability related to ice microphysics aloft? We address these questions using data collected by the NASA NPOL polarimetric radar in conjunction with the surface disdrometer network, aircraft observations, and reanalysis data.

2. Data and methods

a. NPOL

NASA's mobile, S-band polarimetric radar NPOL was stationed on the coast of Washington's Olympic Peninsula (Fig. 1), providing an unobstructed view over the ocean, as well as over the terrain and up the heavily instrumented Quinault River Valley. NPOL performed a series of 360° PPI volume scans and alternating RHI sectors over the ocean (210°–326° azimuth from NPOL) and up the Quinault Valley (30°–60° azimuth from NPOL) every 20 min (Houze et al. 2017; McMurdie et al. 2018). Such a unique scanning strategy provided detailed vertical structure information over both the ocean and the terrain sectors while maintaining a larger spatial coverage area to place the observations in context and regular low-level scans for precipitation estimation. The polarimetric capabilities allow for estimation of bulk hydrometeor characteristics, precipitation phase discrimination, DSD characteristics such as median size (D_0) and normalized number concentration (N_w), and precipitation rate (RR). The data used in this study were quality controlled and processed by NASA (Wolff et al. 2017) unless specifically discussed below. Beam-blockage from terrain is a challenging problem in this region. Reflectivity (Z) and Z_{dr} in the low-level PPIs were corrected following Lang et al. (2009) using both a digital elevation model (DEM) and polarimetric self-consistency (the blockage patterns are shown in the supplementary material). Data were gridded (both RHI and PPI) for certain applications herein using Cartesian interpolation to 1 km spacing in x and y and 0.5-km spacing in the vertical with RadX2Grid software (https://ral.ucar.edu/projects/titan/docs/radial_formats/radx.html).

1) DSD AND RAINFALL ESTIMATION

Given the concentration of observations along the Quinault Valley, Hovmöller diagrams were created in a latitude band extending from 47.2° to 47.6° (see shaded band in Fig. 1) by taking a mean for the surface data from the PPI scans over all points within the latitude band. Similarly, time–height analyses were created by taking the mean in the same latitude band at each grid height using the gridded RHI sectors for land and ocean.

Polarimetric radar provides estimates of particle sizes, number concentrations, improved rainfall rates, and bulk hydrometeor types, essential components to understanding precipitation processes and the relative impacts of terrain, microphysical processes, and synoptic regimes. Here we use the median drop diameter (D_0 in mm) and the normalized intercept parameter (N_w; m^{-3} mm^{-1}; $\log N_w$ will be used hereafter) to characterize the drop size distribution (DSD; Ulbrich 1983; Willis 1984). The formulation for N_w (m^{-3} mm^{-1}) is

$$N_w = \frac{3.67^4 10^3 \text{LWC}}{\pi \rho_w D_0^4}, \tag{1}$$

where the liquid water content (LWC) is in g m^{-3}, and ρ_w is the density of water (1 g cm^{-3}). These parameters were calculated from NPOL polarimetric data by Wolff et al. (2017).

Finally, the radar spectrum width (SW) can be useful in understanding air motions and their relationship to microphysical processes (Houze and Medina 2005; Barnes et al. 2018). SW is the square of the second moment of the Doppler velocity measurement. Regions of strong turbulence and shear act to broaden SW (Doviak and Zrnic 2006).

Disdrometer data deployed for OLYMPEX were used to create rain rate estimators as a function of Z, Z_{dr}, and specific
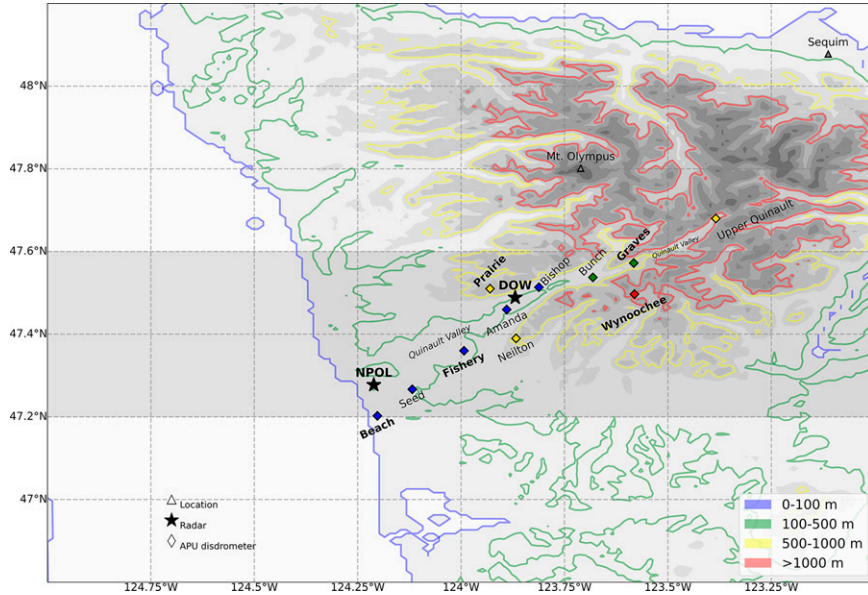
FIG. 1. The Olympic Peninsula and the locations of the APU disdrometers (diamonds), radars (stars), and locations of Sequim and Mt. Olympus (triangles). The terrain is contoured in four elevation bands used in this study highlighted in colors, and the disdrometer symbols are similarly colored by their elevation band. The disdrometers used in detail for the analysis are in boldface font. The darker gray shaded box denotes the latitude band used for the Hovmöller diagrams.

differential phase (K_{dp}) (Table 1). It bears noting that these relationships do not deviate significantly from other previously published relationships, particularly those of Brandes et al. (2002). Instead of applying a single relationship to all raining points, so-called blended rainfall algorithms select the appropriate rain estimator given the hydrometeor type at a gridpoint and thresholds on the polarimetric variables (e.g., Cifelli et al. 2011; Chen et al. 2017; Rutledge et al. 2019). Several studies have shown that this type of algorithm statistically outperforms single rain estimators in comparison to surface observations (e.g., Cifelli et al. 2011; Chen et al. 2017; Jackson et al. 2021). In this regime, the algorithm attempts to use $R(K_{dp}, Z_{dr})$ if $K_{dp} > 0.3°$ km^{-1}, $Z_{dr} > 0.25$ dB, and $Z > 38$ dBZ. If the K_{dp} and Z thresholds are not met, the algorithm uses $R(Z, Z_{dr})$ and if Z_{dr} is not satisfied but K_{dp} and Z are, it uses $R(K_{dp})$. Finally, the algorithm defaults to $R(Z)$ if none of the above thresholds are met. The algorithm uses the hydrometeor identification algorithm to apply the estimation to only points with liquid only (rain or light rain). Note that these thresholds depend on radar wavelength and are appropriate for S-band. In this region, the $R(Z)$ estimator is used most

TABLE 1. S-band rainfall-rate estimation equations for the OLYMPEX project. Note that Z_h and ζ_{dr} are the linear forms of reflectivity and Z_{dr} in these equations.

Equation	a	b	c
$Z_h = aR^b$	145	1.709	—
$R = aZ_h^b \zeta_{dr}^c$	0.012	0.887	−4.563
$R = aK_{dp}^b$	42.5	0.723	—
$R = aZ_{dr}^b K_{dp}^c$	110	−2.171	0.934

frequently, but occasionally $R(K_{dp})$ and $R(Z, Z_{dr})$ are employed, but rarely all three thresholds were met, so $R(K_{dp}, Z_{dr})$ was minimally used due to K_{dp} remaining small at S-band.

2) HYDROMETEOR CLASSIFICATION ALGORITHM (HCA)

Hydrometeor identification algorithms have been used to infer bulk characteristics of hydrometeors within a radar volume. Thompson et al. (2014) developed a fuzzy logic hydrometeor classification (HCA) specifically for cold-season applications. This algorithm differentiates between ice crystal types including dendrites (DN) and plates (PL), in addition to aggregates (AG) and ice crystals (IC). Instead of relying on an external temperature profile such as a sounding or reanalysis data, the HCA uses polarimetric data to locate the melting layer (Giangrande et al. 2008), allowing for better classifications when the bright band is not homogenous or concentric within the radar domain, which is often the case during synoptic systems impinging on the complex terrain of the Olympic mountains. The HCA identifications are representative of the *dominant* hydrometeor type within a volume. The classifications will be evaluated against in situ data from aircraft in section 3b. To synthesize the results of the HCA, the frequency of each type identified in a given latitude band (or height level) are obtained from the RHI volumes over the ocean and land sectors.

b. Disdrometers

To capture the high spatial variability of rainfall within the complex terrain, a large number of surface disdrometers were placed at different locations in the terrain as well as the coastal plain during OLYMPEX. Herein we use 11 Automated Parsival

TABLE 2. APU locations, elevations, and relative location to NPOL. The disdrometers selected to represent each terrain band are denoted in boldface italics.

Name	Lat (°N)	Lon (°E)	Elev (m)	Terrain band	Distance from NPOL (km)	Azimuth from NPOL (°)
Beach (BE)	*47.202 533*	*−124.202 342*	*4.6*	*Ocean*	*8.3*	*175.4*
Fishery (FI)	*47.359 944*	*−123.993 067*	*52.0*	*Coast*	*18.8*	*60.7*
Amanda	47.459 558	−123.889 753	64.0	Coast	31.3	49.9
Seed	47.266 642	−124.118 067	79.3	Coast	7.12	99.5
Bishop	47.513 542	−123.811 894	85.0	Coast	40.0	48.7
Bunch	47.537 411	−123.681 375	115.8	Middle	49.3	53.8
Graves (GR)	*47.572 069*	*−123.582 544*	*180.0*	*Middle*	*57.5*	*55.0*
Prairie (PR)	*47.51*	*−123.93*	*543.0*	*High*	*33.4*	*39.2*
Upper Quinault	47.679 853	−123.384 128	640.1	High	76.6	53.9
Neilton	47.389 839	−123.867 039	656.8	High	28.0	64.1
Wynoochee (WY)	*47.496 889*	*−123.580 889*	*1020.0*	*Tops*	*53.3*	*62.5*

Disdrometers (APUs; Petersen et al. 2017) located along the Quinault Valley (Fig. 1, Table 2). These optical disdrometers detect falling particles through disruption of a wide laser, which then provide size and fall velocity information in 32 unequally spaced size bins. The raw data were processed using the quality control method and particle classification algorithm from Friedrich et al. (2013) to account for specific errors associated with Parsival disdrometers, including wind errors, splashing effects, and margin fallers. In conditions with strong winds, drops tend to pass through the horizontal laser at a large angle from zenith, which results in smaller fall speeds for large drops. Thus, the quality control method removes large drops with small fall speeds. Splashing effects occur when heavy rainfall impacts the two disdrometer heads and cause droplet breakup into a large concentration of smaller drops. Margin fallers are drops that pass along the edge of the wide laser, and thus appear as smaller drops with large fall speeds (Friedrich et al. 2013). This method removes rain drops whose fall speeds are 60% larger or smaller than the expected fall speed relationship for rain as was done in Friedrich et al. (2013). The data were filtered to remove snow particles from rain using a fall–velocity–size relationship; however, some mixed phase particles (such as snow pellets) are included in the analysis presented. Some APUs have periods of missing data due to power drops, corrupted data, etc.

c. Terrain bands

To examine the orographic impacts as a function of terrain height, the NPOL domain was divided into five bands: Ocean (<5 m), Coast (5 < elevation < 100 m), Middle (100 < elevation < 500 m), High (500 < elevation < 1000 m), and Tops (>1000 m) MSL. Each NPOL surface grid point was categorized based on the DEM. A representative disdrometer within each height band is used for comparison. These disdrometers were determined based on their favorable locations and data reliability. For the Ocean band, Beach was selected given the proximity to the ocean and a height of 4.6 m MSL (Table 2). Fishery (52 m) is representative of the Coast, Graves (180 m MSL) falls into the Middle terrain band, Prairie (543 m MSL) represents the High band, and finally, Wynoochee was at an elevation of 1020 m, in the Tops terrain band. These disdrometers were also at varying distances inland along the Quinault

Valley, providing an approximate transect of precipitation as it moves inland (Fig. 1, Table 2).

3. Scientific results

a. Precipitation variability

The OLYMPEX assets were deployed during the 2015 IOP (November–December 2015) to capture synoptic systems which included several atmospheric river (AR) events
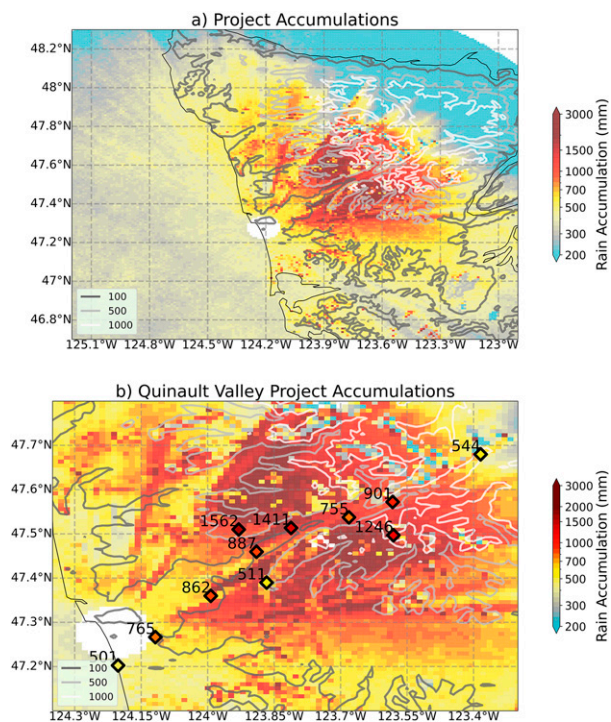

FIG. 2. (a) NPOL surface rainfall accumulation for the time period from 12 Nov to 19 Dec. (b) As in (a), but zoomed in on the Quinault Valley with disdrometer accumulations (colored the same as the color bar and accumulations in mm labeled with text). Terrain is contoured in dark gray (100 m), silver (500 m), and white (1000 m), and the coastline is outline in black.
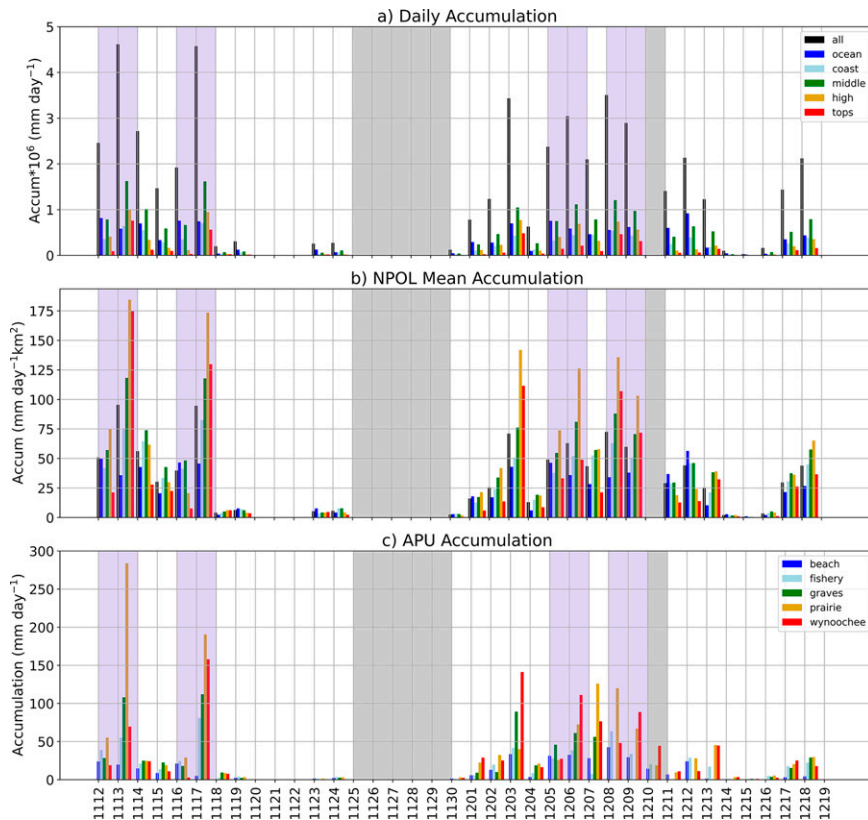
FIG. 3. Time series of daily NPOL rain accumulations as a function of terrain for the 12 Nov–19 Dec period of OLYMPEX over the domain given in Fig. 1. (a) Total accumulation from all grid points in each terrain band; and (b) mean accumulation per km^2 (total accumulation divided by the total area in each band) from NPOL data. (c) Daily rain accumulations from the APU disdrometers at different terrain heights. Gray shading indicates times when NPOL was not operating. Purple shading indicates four periods selected for case studies.

(Houze et al. 2017). This leads to a rich dataset to examine the impacts of environment, synoptic regime, microphysics, and terrain in generating precipitation in this area.

OLYMPEX precipitation accumulations from November to December 2015 show significant enhancement in the terrain at the Middle to High elevations (Fig. 2, gray and silver contours), in agreement with prior studies (Houze et al. 2017; Zagrodnik et al. 2018). In fact, from a surface rainfall accumulation map, it is clear that the Olympic mountains received at least twice as much precipitation (over 2000 mm in some places) compared to the nearby ocean, where project accumulations were below 600 mm. Due to beam blockage and curvature effects at longer ranges from NPOL (>100 km) where the beam may actually be above the melting level, it is difficult to quantify the effect of the rain shadow in the lee of the Olympic Mountains, but is consistent with the Mass and Ferber (1990) climatology showing an order of magnitude less accumulated precipitation than over the highest terrain (Fig. 2, white contours) and the lee side of the Olympics. Purnell and Kirshbaum (2018) reached a similar conclusion. Both NPOL analysis and the disdrometers show that the Middle and High (100–1000 m) sites such as Prairie and Wynoochee, generally accumulated the most rainfall over

the project (Fig. 2b), in comparison to the Coastal (<100 m) and Tops (>1000 m). In addition, one low-elevation site (Bishop) in the Quinault Valley shows relatively high rainfall accumulations (1411 mm) over the project as the influence of the surrounding higher topography and strong orographic effects impact the resulting campaign-long rain accumulation (Fig. 2b; also described in Houze et al. 2017; Zagrodnik et al. 2018). These results demonstrate that terrain height is not the most important factor in determining total precipitation over this area.

Widespread precipitation fell during the OLYMPEX period, with measurable rainfall within the domain (defined in Fig. 1) on 28 of the 33 days NPOL was operating in November and December (Fig. 3). Several of these days stood out with significant accumulated rain over the entire domain, including 13 and 17 November and 3, 5, and 8 December (Fig. 3a). These were all AR events, and in fact, the 17 November and 9 December led to a significant rise in the level of Lake Quinault and subsequent flooding (Houze et al. 2017). If we consider the mean accumulation per square kilometer in each band, the High terrain notably accumulates the largest mean rainfall on 11 days, indicating that it is likely raining harder and/or for longer periods of time

TABLE 3. Overview of the four cases examined in the text. Boldface font highlights the total time analyzed for each case. The asterisk for cases 1 and 2 denote the passage at NPOL.

Case	Frontal regime	Start time	End time	Total time
Case 1 (12–13 Nov)				**~32.5 h**
	Prefrontal	1200 UTC 12 Nov	0300 UTC 13 Nov	18 h
	WS1	0300 UTC 13 Nov	1000 UTC 13 Nov	7 h
	WS2	1000 UTC 13 Nov	1400 UTC 13 Nov	4 h
	WS3	1400 UTC 13 Nov	1715 UTC 13 Nov	3 h 15 min
	NCFR	1715 UTC 13 Nov*		
Case 2 (16–17 Nov)				**~24.5 h**
	Warm front	2100 UTC 16 Nov	0000 UTC 17 Nov	3 h
	WS1	0000 UTC 17 Nov	0600 UTC 17 Nov	6 h
	WS2	0600 UTC 17 Nov	0900 UTC 17 Nov	3 h
	WS3	0900 UTC 17 Nov	2130 UTC 17 Nov	12 h 30 min
	NCFR	2130 UTC 17 Nov*		
Case 3 (5–6 Dec)				**~42 h**
	Postfrontal	0000 UTC 5 Dec	0700 UTC 5 Dec	7 h
	Prefrontal	0800 UTC 5 Dec	1700 UTC 5 Dec	10 h
	WS1	1700 UTC 5 Dec	0600 UTC 6 Dec	13 h
	WS2	0600 UTC 6 Dec	0800 UTC 8 Dec	2 h
	WS3	0800 UTC 6 Dec	1800 UTC 6 Dec	10 h
Case 4 (8–9 Dec)				**~43 h**
	Postfrontal	0000 UTC 8 Dec	0700 UTC 8 Dec	7 h
	Prefrontal	0700 UTC 8 Dec	1500 UTC 8 Dec	8 h
	Frontal	1500 UTC 8 Dec	2000 UTC 8 Dec	5 h
	WS1	2000 UTC 8 Dec	2200 UTC 8 Dec	2 h
	WS2	2200 UTC 8 Dec	0600 UTC 9 Dec	8 h
	WS3	0600 UTC 9 Dec	0900 UTC 9 Dec	3 h
	Cold front	0800 UTC 9 Dec	1800 UTC 9 Dec	10 h

compared to the other bands (Fig. 3b). The Tops band also shows high accumulations in three of the same days. Comparisons to disdrometer accumulations in these terrain bands suggest similar trends, with the 13 and 17 November days standing out with more than 150 mm falling at Prairie (High) (Figs. 3b,c).

There are four cases that stand out with high total accumulations and significant contributions to the rain volume from the moderately elevated terrain bands, indicative of significant orographic enhancements: 12–13 November (case 1), 16–17 November (case 2), 5–6 December (case 3), and 8–9 December (case 4) (Fig. 3, purple shading). While the 3 December case has similar daily characteristics to these four cases, when considering the life cycle of a landfalling frontal system as an event, the four selected cases have much higher accumulations due to their extension over multiple days. We further investigate the orographic, microphysical, and synoptic processes contributing to the precipitation (Table 3) in these four cases, and explore case 2 with detailed analysis of NPOL RHIs.

Time–longitude analysis (Hovmöller diagrams) are presented as a means to characterize the precipitation and environment for the four selected cases. The cases are divided into frontal regimes through reanalysis and sounding analysis following Zagrodnik et al. (2018) and McMurdie et al. (2018). These divisions include well-defined prefrontal stages, large warm sectors, some cold front passages, and postfrontal conditions (see Fig. 8 in Houze et al. 2017 for a conceptual model describing these sectors). In both November cases, the end of the time period of interest was marked by the passage of a well-defined narrow cold-frontal

rainband (NCFR; Parsons and Hobbs 1983). The postfrontal sector from a previous system was included as part of both cases 3 and 4 for comparison purposes to the other synoptic regimes. These periods are more isolated and convective in nature, with generally low rain rates.

MERRA2 was used to analyze the moisture, winds, and temperature fields over the domain (Fig. 4). IVT was calculated following Gao et al. (2015) on the mandatory levels. The November cases are characterized by large IVT during a long period (Figs. 4a,b), while the December cases have shorter periods of large IVT during the warm sector (Figs. 4c,d). Cases 1, 2, and 4 are all AR events with southwesterly flow, turning westerly with time. In these cases, the flow brings substantial moisture directly into the Quinault Valley. The dependence on flow direction has been shown to be critical for the orographic enhancement (McMurdie et al. 2018; Zagrodnik et al. 2018) and rain shadow effect in the lee of the Olympic Mountains (Siler et al. 2013). Case 3 stands out with slightly lower IVT values than the other cases, and southerly flow at 850 hPa throughout the period over the entire domain (Fig. 4c). Thus, although there is still over 400 kg s^{-1} m^{-1} of IVT, the 850-mb winds were not directed into the terrain, and particularly the Quinault River Valley, as in the other cases. Cases 1, 2, and 3 are characterized with low freezing levels (<1.5 km) initially, which rise to over 2 km in the warm sector (Figs. 4e–g). Case 4 has initially higher melting layers (>2.0 km) which lower after the passage of a cold front at the end of the period around 0900 UTC 9 December (Fig. 4h).
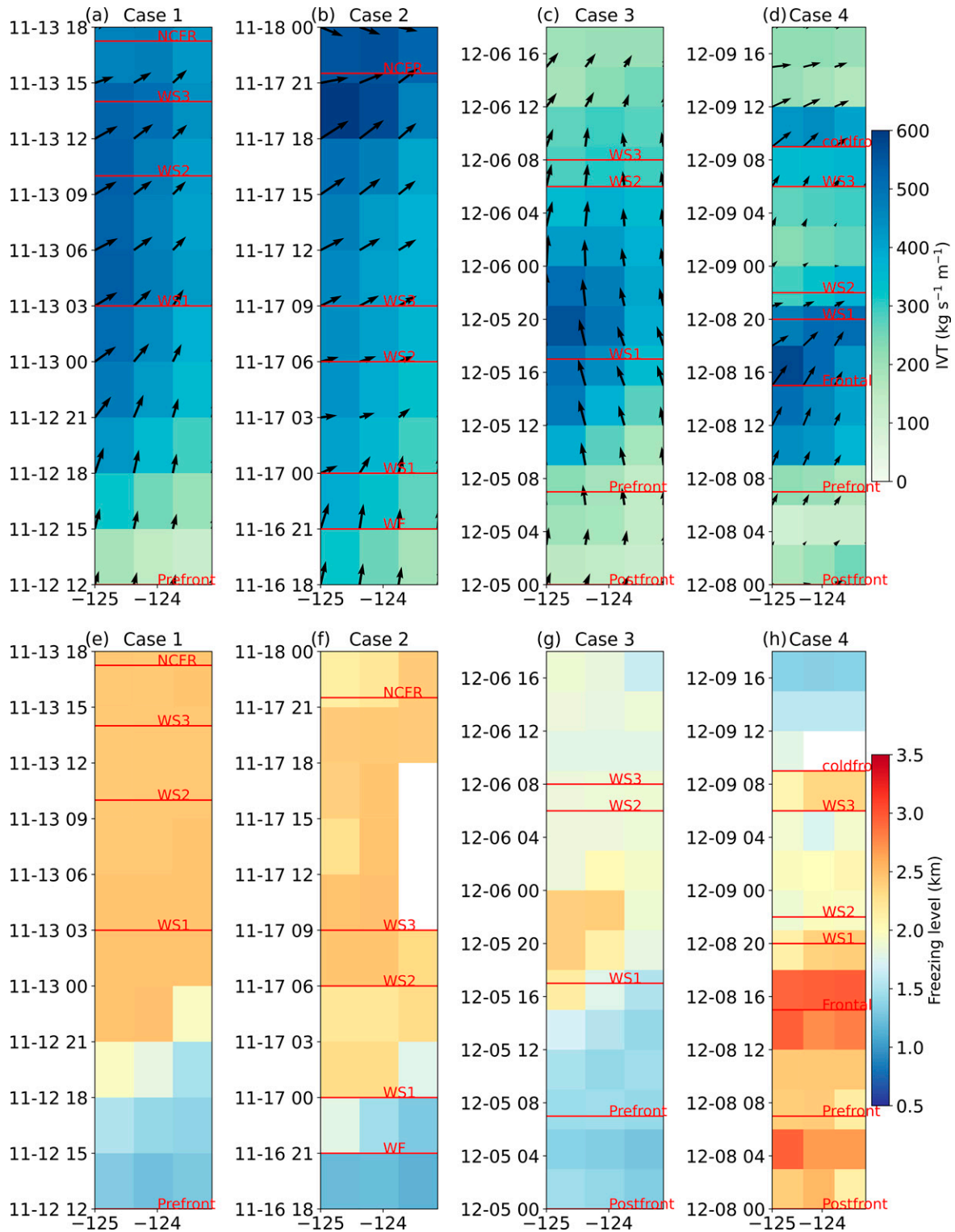
FIG. 4. Overview of the environmental conditions for each case presented as Hovmöller diagrams derived from MERRA2 data over the latitude band highlighted in Fig. 1. (top) The integrated vapor transport (IVT) with the 850-hPa winds overlaid and (bottom) the 0°C freezing level. Synoptic periods are indicated in red.
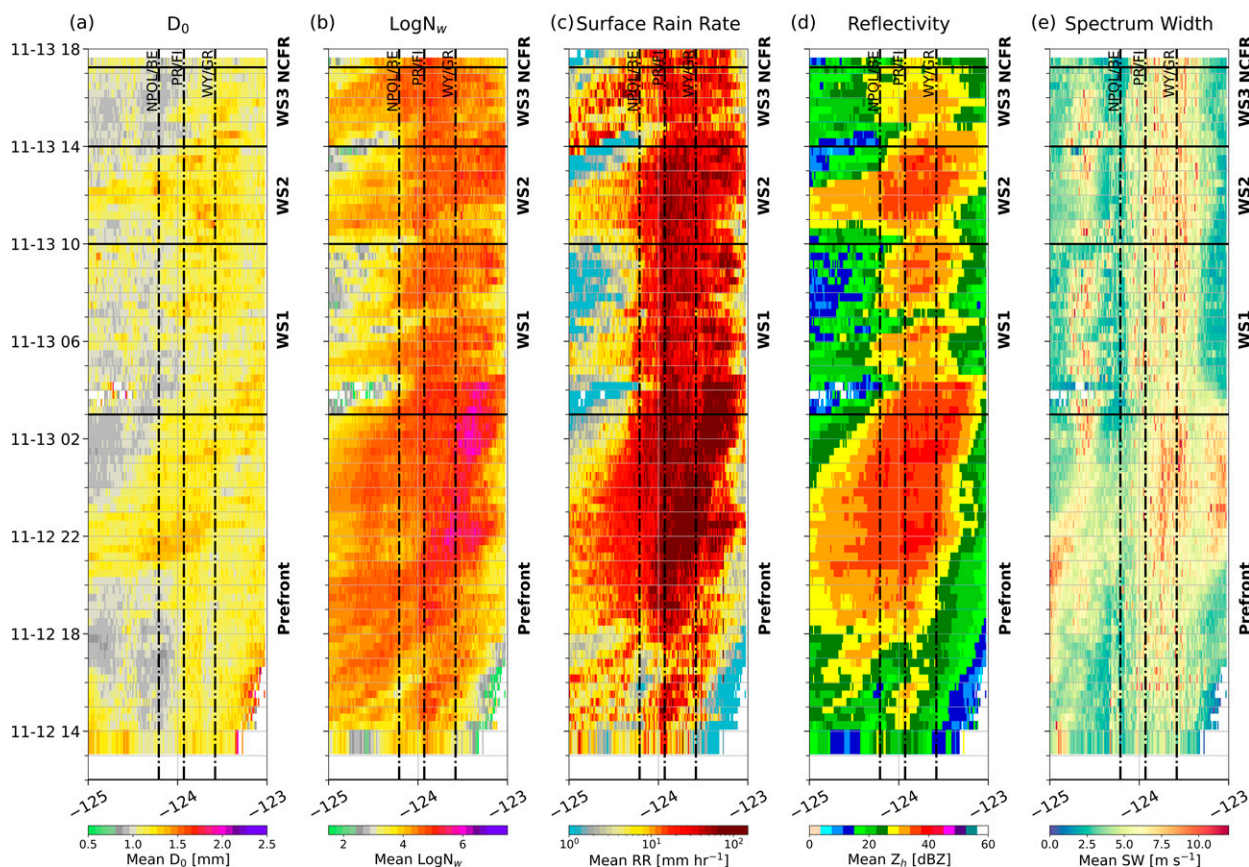
Case 1 Nov 12-13

FIG. 5. Hovmöller diagrams of NPOL-derived surface mean (a) D_0, (b) logN_w, (c) rain rate, (d) reflectivity, and (e) spectrum width for case 1, 12–13 Nov 2015. The synoptic periods are denoted with black horizontal lines, and the approximate longitudes of the disdrometers and NPOL are indicated with dashed–dotted vertical lines.

In all cases, the mean rain rates are largest and most continuous over the terrain (Figs. 5–8). In cases 1 and 3, the prefrontal periods are characterized by widespread moderate rain rates (1–5 mm h^{-1}) over the ocean, and heavier rain rates (10–25 mm h^{-1}) impinging on the steep terrain (Figs. 5 and 7). These periods have significantly high logN_w (>5) and elevated mean D_0 (>1.2 mm) over the highest terrain, including Prairie and Wynoochee sites. The prefrontal period of case 3 has relatively light mean rain rates (<3 mm h^{-1}) over the ocean and small D_0 (<1.0 mm) but higher mean rain rates (>5 mm h^{-1}) over the terrain with uniformly high logN_w (>5) and larger D_0 (1.0–1.4 mm) (Fig. 7). Case 4 has continuous heavy rainfall (>10 mm h^{-1}) over the terrain with lighter periods over the ocean (Fig. 8). Mesoscale variability was present in each case, especially within the warm sector where several distinct patterns in rain rate and DSD parameters are evident. Zagrodnik et al. (2018) found that mesoscale features were often associated with significant changes to the DSDs observed by the disdrometers, and therefore the warm sectors are divided into mesoscale periods. For example, in all cases, the initial warm sector (WS1) is characterized by widespread mean rain rates >3 mm h^{-1} over both the ocean and land (Figs. 5c, 6c, 7c, and 8c). Several cases

have a period of significantly decreased rain rates over both the terrain and ocean, denoted as Warm Sector 2 (WS2), case 2 and case 3; (Figs. 6c and 7c) which are characterized by smaller D_0 and lower logN_w. In the final phase of the warm sector (WS3), heavier rain returns, again focused on the terrain, most notably in cases 2 and 3 (Figs. 6c and 7c). In all four cases, the heavier mean rain rates (>10 mm h^{-1}) are generally focused over the terrain through the duration of the warm sector, supporting the findings of Zagrodnik et al. (2018), Purnell and Kirshbaum (2018), and McMurdie et al. (2018), who found the greatest orographic enhancement in the warm sector. The Hovmöller analysis of these cases suggest a preference for increased SW (and therefore, turbulent motions) at the longitude of Wynoochee and Graves sites, likely resulting from the shear and drag encountered as the air mass is forced inland against the steep terrain. In addition, generally larger logN_w are more frequent over the Prairie, Fishery, Graves, and Wynoochee longitudes in comparison to the longitudes of the ocean sector and Beach site across all regimes. Finally, these cases show nearly continuous mean rain rates above 5 mm h^{-1} at longitudes between Fishery and Wynoochee during most synoptic regimes, while the variability over the ocean is much larger.
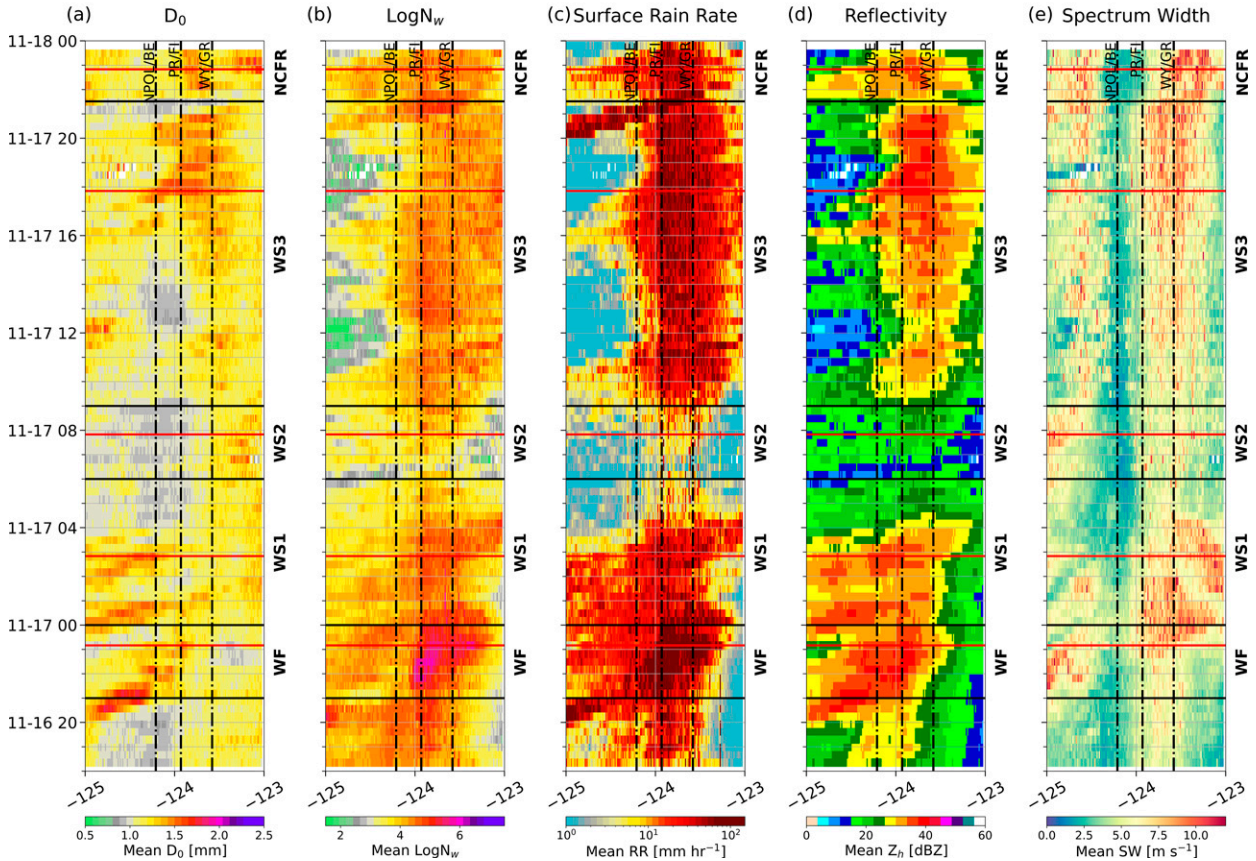
Case 2 Nov 16-18

FIG. 6. As in Fig. 5, but for case 2, 16–17 Nov 2015. Red horizontal lines indicate the times of the RHI analysis presented in section 3d.

b. Microphysical variability

The microphysical analysis herein relies heavily on the HCA. Therefore, we begin with a brief evaluation of the HCA using in situ observations from the University of North Dakota (UND) Citation II aircraft equipped with particle imagers, temperature, and liquid water content (LWC) measurements. For several cases where the Citation performed flight legs or spirals over the Quinault Valley, data from the 2D particle imagers were compared to the HCA classifications and polarimetric radar data from vertical cross sections nearby in time and space (Delene 2017; Heymsfield et al. 2017; Poellot et al. 2017). An example from the 5 December flight, where the Citation performed a "profiling" spiral from 1500 to 1515 UTC over the Doppler on Wheels (DOW) radar, is shown in Fig. 9. The LWC from the Nevzorov probe (Fig. 9a) shows water contents reaching 0.05 g m^{-3} around 3 km and generally decreasing with height. The ice water content (IWC) reaches a maximum of 1.0 g m^{-3} with generally decreasing values with height (Fig. 9b). Both IWC and LWC have relative maxima in a layer near 4.5 km, corresponding to a temperature of −13°C. Images from the CP2 probe of individual crystals show stellar crystals and plates with dendritic extensions (Fig. 10; 1505 UTC). The 2DSH shows fewer but larger crystals mixed in

with some small water droplets. This is all consistent with the favored growth of pristine plate-like crystals in environments with ice supersaturations between −10° and −15°C (Pruppacher and Klett 1997). The HCA classifies a layer of PL at this same level, consistent with larger particles with high axis ratios. Many of the crystals exhibit riming, indicative of the high LWC and possibly increasing the bulk density of these type of crystals to push them into the PL classification (as compared to a DN category which would have slightly smaller Z_{dr} and K_{dp} values, but we note there is significant overlap in the algorithm's membership beta functions that drive the fuzzy logic scoring of these two categories). At warmer temperatures lower in the cloud, the CP2 and 2DS show prolific small columns with some riming and aggregation (Fig. 10, 1500 and 1501 UTC). The HCA at this level shows mainly AG classifications. As temperatures reach −10°C around 4 km, the crystal growth mode changes to larger dendrites and plates (Fig. 10, 1503 UTC) with some bullet and columnar extensions. The HCA starts to identify some PL mixed with the AG. Above 5 km at temperatures colder than −15°C, LWC are less than 0.005 g m^{-3}, and IWC are less than 0.2 g m^{-3}. CP2 images from these levels indicate numerous heavily rimed bullet rosettes and some plates (1506–1510 UTC, Fig. 10),
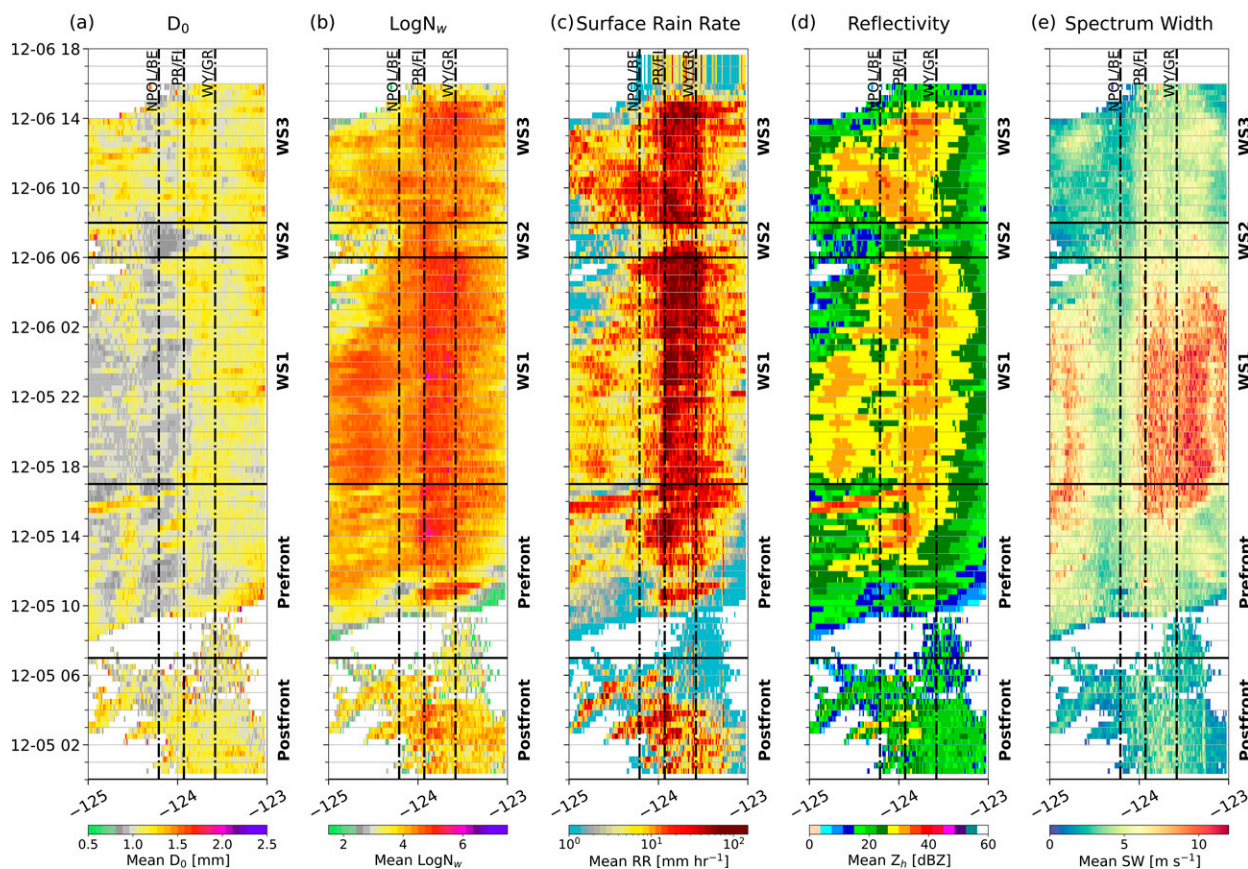
Case 3 Dec 05-06

FIG. 7. As in Fig. 5, but case 3, 5–6 Dec 2015.

and even some larger spherical—possibly liquid—drops are identifiable on the 2DSH. Near the top of the cloud, single columns, hollow columns, and clumps of columns are frequent (Fig. 10, 1511–1513 UTC). In this region the HCA identifies primarily IC.

These observations, in addition to other concurrent aircraft data and HCA, demonstrate that the HCA identifications generally align with their inferred categories as synthesized in Fig. 9c. We note that none of the data examined included a flight through a region of pristine dendrites as identified by the HCA, but the distinction between the PL and DN in the HCA is slightly larger reflectivities, larger K_{dp} values, and slightly lower Z_{dr} values for DN (Thompson et al. 2014). This is indicative of lower density and slightly larger particles more characteristic of branched dendrites compared to more compact and dense stellar or plate crystals. The PL classifications were sometimes associated with rimed dendrites in the probe data, which could increase the bulk density enough to present as PL in the classification. Additionally, many of the plate crystals were stellar crystals with dendritic extensions. Therefore, we acknowledge that the PL category may include particles with characteristics which may allow them to aggregate more readily than a pristine plate crystal.

The discussion henceforth relies on time–height and time–longitude (Hovmöller) analysis of the frequency of HCA

classifications. The relative frequencies of the HCA from the RHIs are calculated by taking the total number of grid points identified for each particle type and dividing by the total number of points with identifications over the time period for the ocean and land separately. Time-height cross sections are composed similarly. Interpretation of the frequencies should therefore be relative to all identified species for land and ocean over the time period separately. We note here that the spatial variability of the HCA particle types as a function of terrain height may not be represented; this is, in fact, difficult to detangle due to advection and the complexity and steepness of the terrain within the averaged area.

In case 1, clear differences in the HCA frequencies between the synoptic regimes are evident, as well as land and ocean contrasts (Fig. 11). During the prefrontal period where rain rates were moderate over the ocean sector (Fig. 5c), there is a relative maximum of AG, particularly below 6 km, most notable over the ocean (Fig. 11l). This is associated with a slightly increased frequency of PL (Fig. 11f), which based on the Citation probe data, could indicate denser, rimed branched plates that readily aggregate. The Beach disdrometer (the closest to representing the "ocean," Fig. 11a) shows some larger particles, although relatively small rain rates (<5 mm h^{-1}). At the end of the
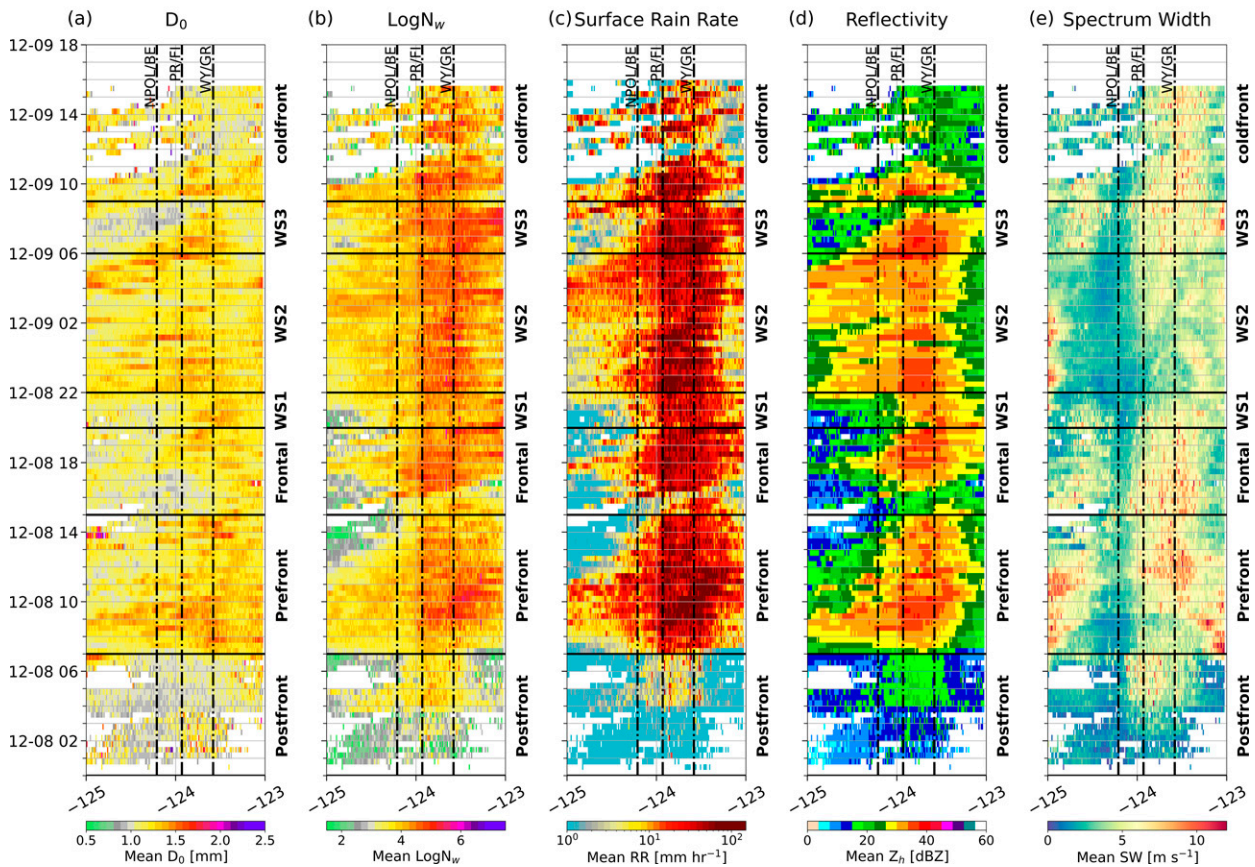
Case 4 Dec 08-09

FIG. 8. As in Fig. 5, but case 4, 8–9 Dec 2015.

Prefrontal period after 0000 UTC 13 November, there is an increase in the frequency of DN, particularly at the longitude of Prairie (Fig. 11j); however, there is no corresponding AG signature. During this time, the Prairie disdrometer (Fig. 11c) shows an increase in rain rates reaching to 20 mm h^{-1}, although this is likely due to an increase in the small drops (<1 mm) following from the high vapor transport as noted by Zagrodnik et al. (2018). There is no apparent response in the DSDs to the DN, suggesting that the surface precipitation is dominated by processes in the warm layer.

As WS1 impinges on the terrain, there is a relative increase in the frequency of DN and associated AG over the land (Figs. 11i–n), while the ocean sector has lower echo top heights (ETH) and lower rain rates. Associated with this is a marked decrease in the mean logN_w over the ocean, but near maximum values of logN_w over all terrain bands (Fig. 5b). During this period, the winds are directly onshore and up the Quinault Valley, and consequently moisture flux is high (Fig. 4a). The disdrometers show small rain rates (1–5 mm h^{-1}) and generally small drops over the coastal plain at Beach and Fishery (Figs. 11a,b), while Prairie has heavier rain with rates generally above 15 mm h^{-1}, a broad size distribution and particularly high concentrations of small drops (Fig. 11c). Rain rates at Graves are lower than Prairie, and

concentrations of small drops are less (Fig. 11d). Again, this suggests enhanced warm rain processes contribute to the surface precipitation during this period because there is no obvious response in rain rate or DSD to the characteristics of the ice identified aloft.

The WS2 period has increased dendritic growth and associated aggregation over land, in particular at the longitude of Prairie/Fishery (Figs. 11j,m), as well as an increase in ETH. During WS2, the rain rates at Prairie are close to 20–25 mm h^{-1}, which is larger than during WS1, and the maximum drop sizes are increased in addition to a depletion of the concentration of small drops. This suggests a response in the surface DSD to the ice microphysics. Larger drops originate as dendrites which then readily aggregate and melt, forming large "seed" drops which continue to collect smaller drops (formed via condensation) as they fall through the 2-km-deep warm layer. This is not the case at the Graves site, which is farther inland but lower in elevation than Prairie (Table 2). WS3 sees a decrease in the DN and AG and lower ice cloud depths as ETHs lower.

As the NCFR moves over the region, it is difficult to discern noticeable changes to the ice frequencies, although the passage is marked in the disdrometers as a sharp decrease in rain rate and lack of large drops preceding the NCFR passage followed
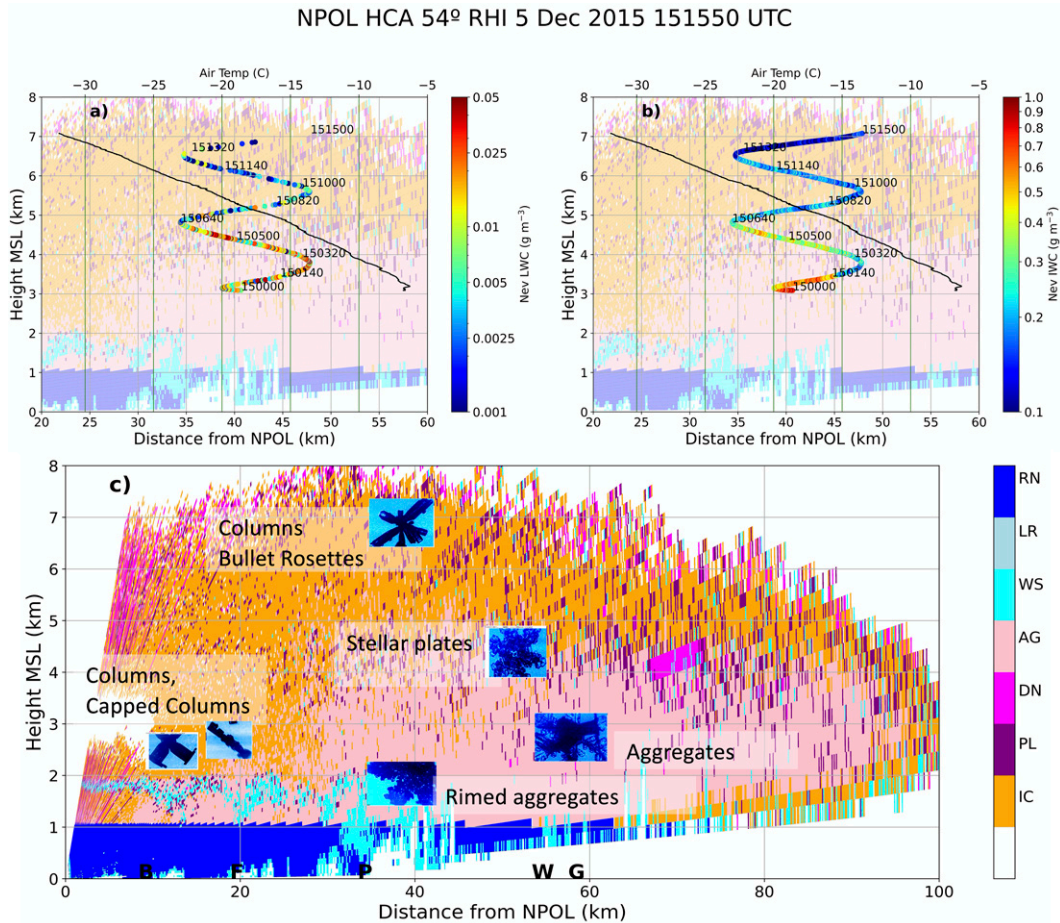
FIG. 9. (a) LWC and (b) IWC from the Nevzorov probe during an ascending spiral from 1500 to 1515 UTC 5 Dec (colored points). The NPOL HCA from an RHI along the DOW (54°) around 1515 UTC is shaded in the background. The air temperature profile is shown in black (top axis). (c) Examples of crystal types in Citation UND Particle Imaging probe relative to the polarimetric radar HCA identifications. The locations of the Beach, Fishery, Prairie, Wynoochee, and Graves disdrometers are represented in black letters. The HCA categories are rain (RN), light rain (LR), wet snow (WS), aggregates (AG), dendrites (DN), plates (PL), and ice crystals (IC).

by a spike in rain rate and general increase in mean sizes as the front moves over each disdrometer (Figs. 11a–e). Frequencies of PL are generally small and comparable between the land and ocean. The Hovmöller of DN (Fig. 11j) suggests some propagation of the dendritic layers from the ocean to the land, although the interactions with the terrain seem to enhance the DN, particularly at distances approximately 25–60 km inland from NPOL.

Case 2 exhibits some of the same characteristics as case 1 (Fig. 12). The DN and AG maximize over the ocean during the WS1 period (Figs. 12i,l), while they are most frequent over the land during the later part of the postfrontal period (Figs. 12k,n). Again, it is notable that the DN and AG frequencies are maximized at the longitude of Prairie (Figs. 12j,m). The WS2 regime is characterized by lower ETH, and a relative decrease in the frequency of large ice species, but high frequencies of small, oriented particles (IC, not shown). Disdrometer DSDs at all locations show this period of light rain was characterized by

only concentrations of small drops rarely exceeding 1.5–2 mm. These drops are likely grown in the warm layer through cloud drop self-collection (Zagrodnik et al. 2021). The largest mean SW values (Fig. 6e) are during WS1 and during and after the NCFR passage suggesting the presence of convective-scale vertical motions, and do not show discernable trends with the overall ice species frequencies. The passage of the NCFR at each site was coincident with a decrease in the rain rate and absence of large drops, followed by a return to moderate rain rates (~5 mm h^{-1}) and a broad size distribution (Figs. 12a–e).

Throughout most of the WS3 period there are increased frequencies of PL over the ocean, indicative of slightly larger but higher bulk density plate-like crystals (Figs. 12f,g). In the later part of the postfrontal period, starting about 1500 UTC 17 November, higher frequencies of DN and AG are noted over the terrain (Figs. 12j,k,m,n). This is accompanied by high rain rates reaching 30 mm h^{-1} over the higher and more inland disdrometer sites (Prairie, Graves, Wynoochee), and
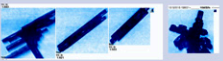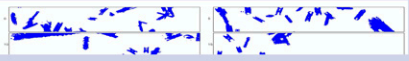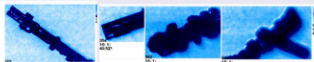
Time (UTC)	CP2 Images	2DSH (buffer 1280µ)	Temperature (ºC)	Altitude (km)
1500			-6.0	3.1
1501			-6.5	3.2
1503			-9.7	3.8
1505			-12.6	4.4
1506			-14.3	4.6
1508			-18.1	5.2
1510			-21.8	5.7
1511			-24.0	6.0
1513			-27.6	6.5

FIG. 10. Data from the 1500–1515 UTC 5 Dec 2015 UND Citation spiral. Images from the CP2 and 2DSH probes are shown for different times along with the temperature and altitude.

an increase in the maximum size of drops, although there is also a coincident increase in the concentrations of little drops, suggesting significant warm-rain contributions to the surface precipitation (Figs. 12c–e).

Case 3, which was characterized by southerly winds, shows less spatial and temporal variability in DSDs, rain rates, and HCA frequencies (Fig. 13). Similar frequencies of hydrometeor types are noted over the land and ocean, with generally low rain rates (<5 mm h^{-1}) during all periods at all sites, except during WS2 at Prairie and the latter half of WS1 at Wynoochee (Figs. 13a–e). There is a distinct propagation of a dendritic layer from the ocean to the terrain between 1500 and 1700 UTC associated with a mesoscale front (Fig. 7), although the influence on the surface DSDs is not obvious. WS1 shows frequent AG over both land and ocean, with corresponding larger particles in the DSDs (up to 3–4 mm, Figs. 13a–e). WS1 also has high mean SW (the highest of all cases and periods), resulting from strong shear and the development of Kelvin–Helmholtz (K–H) waves as the southerly flow interacted with the terrain. This may have increased aggregation through turbulent motions (e.g., Barnes et al. 2018), thereby leading to the presence of larger drop sizes below the melting layer, particularly at Wynoochee (Figs. 13e,n). As in other cases, there is a period of DSDs with high concentrations of small drops with maximum drop sizes of around 1.5 mm at all sites, with Prairie rain rates increasing to 10 mm h^{-1} (Fig. 13c). The HCA frequencies show a lack of associated ice processes, pointing to prolific warm rain processes during this period. Since this case was characterized by southerly winds

which are less favorable for moisture transport directly up the Quinault Valley (Fig. 4c), the flow pattern may have led to decreased liquid water concentrations due to shadowing by the southern mountains as shown by modeling studies (Zagrodnik et al. 2021).

The final case (case 4) shows subtle differences between land and ocean and synoptic regimes (Fig. 14). Again, there is notable propagation of DN layers onshore (Figs. 14i–k), with a preference for increased DN frequencies along the longitude of Prairie. There are more frequent occurrences of PL over the ocean sector during the prefrontal (0700 UTC 8 December) and WS1 and WS2 (20–24 UTC 8 December, Figs. 14f–h). These times are associated with local increases in the AG (Figs. 14l–n), and although plates do not readily form aggregates, these could be higher bulk density rimed dendritic crystals or possibly have some branches, which more readily aggregate with one another. The large concentrations of small drops characteristic of the orographic enhancement are evident during the prefrontal and frontal periods at Fishery and Prairie (Figs. 14b,c), and in fact the highest rain rates at Prairie are during the frontal period (1500–2000 UTC 8 December), extending to nearly 30 mm h^{-1} at times. WS3 shows enhanced DN and AG, and during the same period the maximum sizes of the rain drops increase over Wynoochee, although the increase in rain rate is more correlated with an increase in the concentration of drops smaller than 1 mm. As with the other cases, the AG frequency is maximized over the Prairie longitude (Fig. 14m).
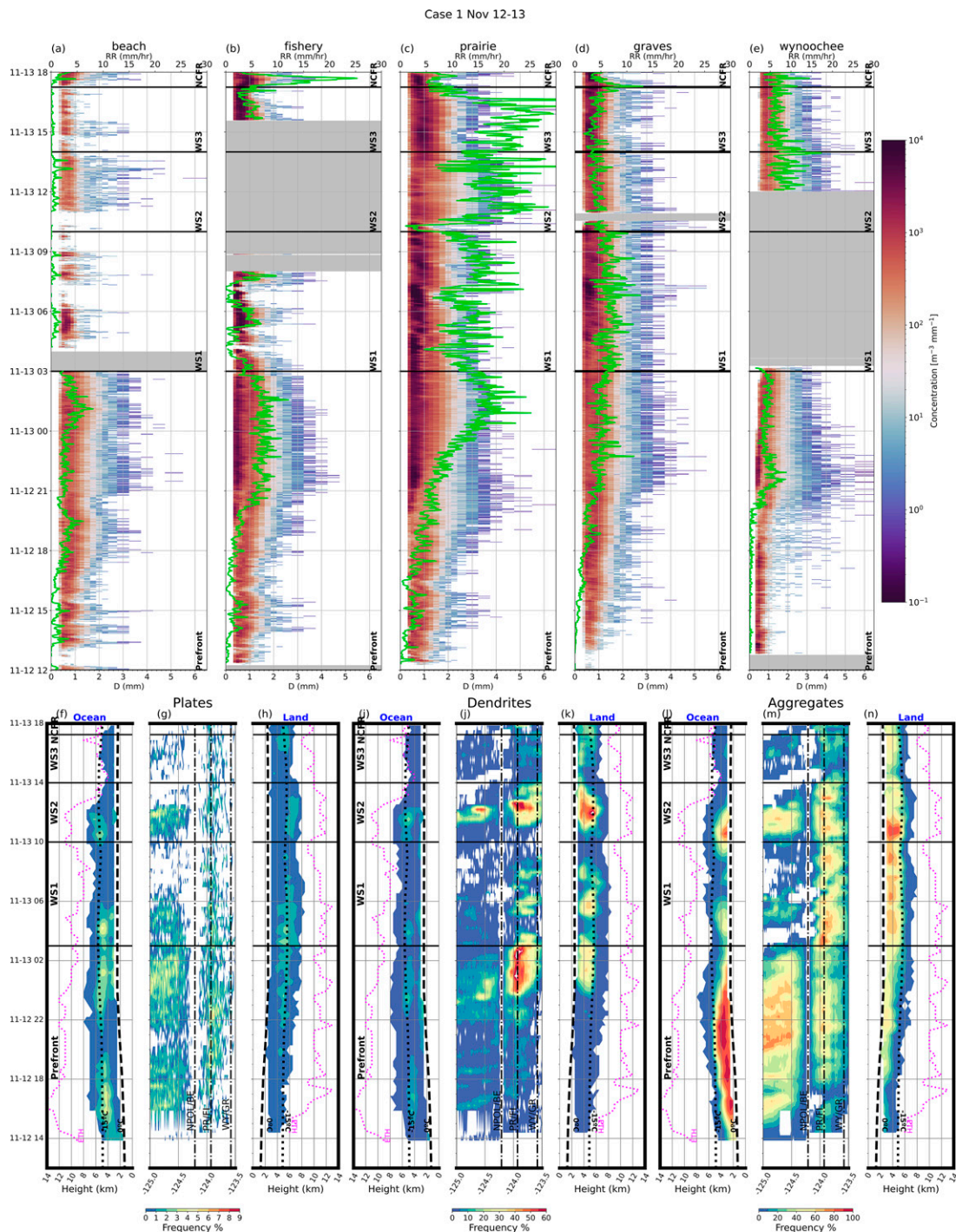
FIG. 11. (a)–(e) Drop concentration (color contours) as a function of drop bin and time for the five disdrometer sites (a) Beach, (b) Fishery, (c) Prairie, (d) Graves, and (e) Wynoochee. A 5-min-smoothed rain rate is plotted in green (top x axis). Periods with missing or bad data are denoted by gray shading. (f)–(n) The relative frequency of HCA classifications for (f)–(h) plates, (i)–(k) dendrites, and (l)–(n) aggregates. Each hydrometeor set shows a time–height plot of (left) the ocean RHIs, (center) Hovmöller, and (right) the land RHIs. The 0° and −15°C isotherms are denoted with black dashed and dotted lines, respectively, on the time–height plots, and echo-top heights are shown by pink dotted lines. The location of the disdrometer longitudes are marked by dashed–dotted lines on the Hovmöller diagrams. Mesoscale and frontal periods are denoted by horizontal black lines and labeled in black.
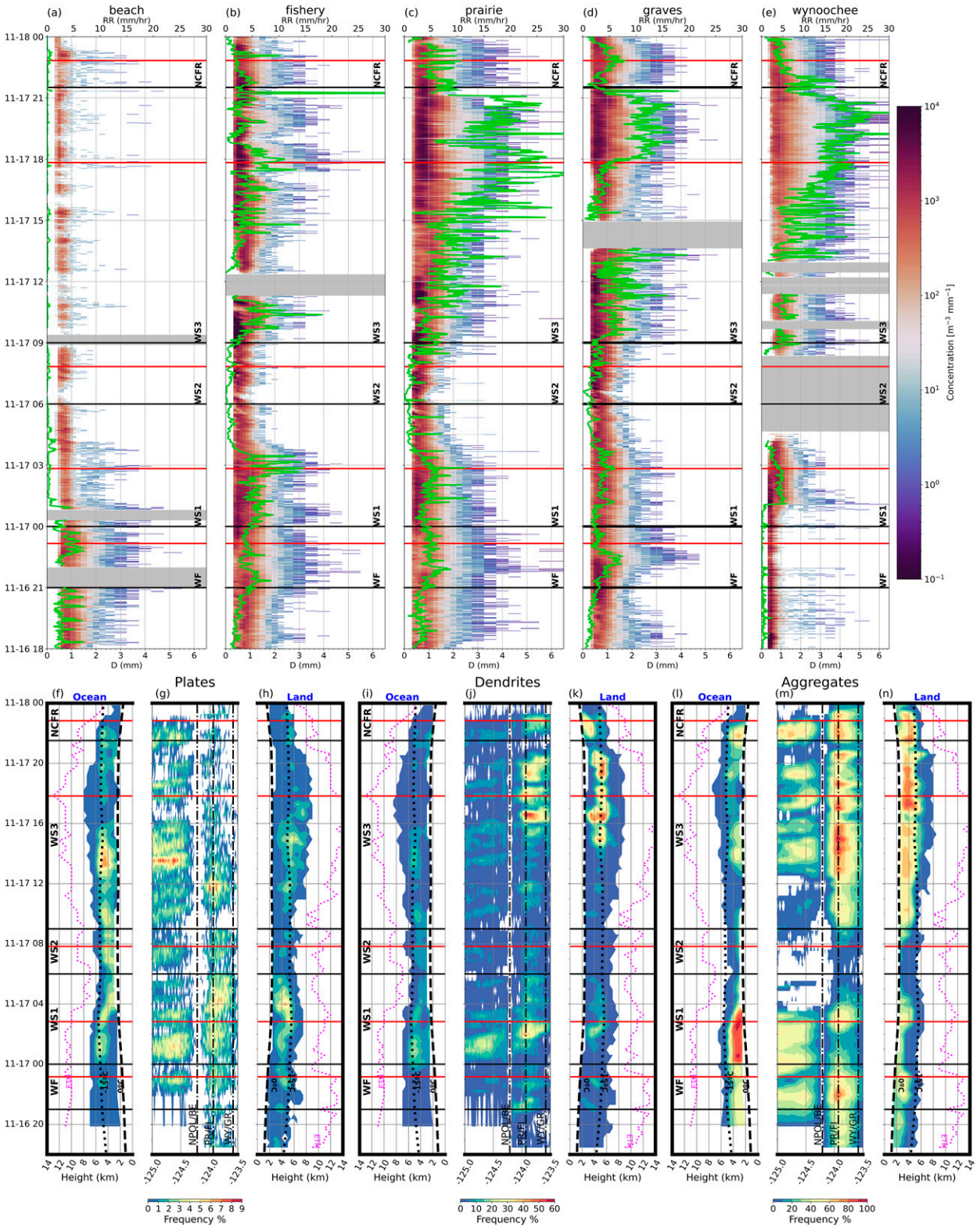
Case 2 Nov 16-18

FIG. 12. As in Fig. 11, but for case 2, 16–18 Nov 2015. Red horizontal lines indicate the approximate RHI times analyzed in section 3d.
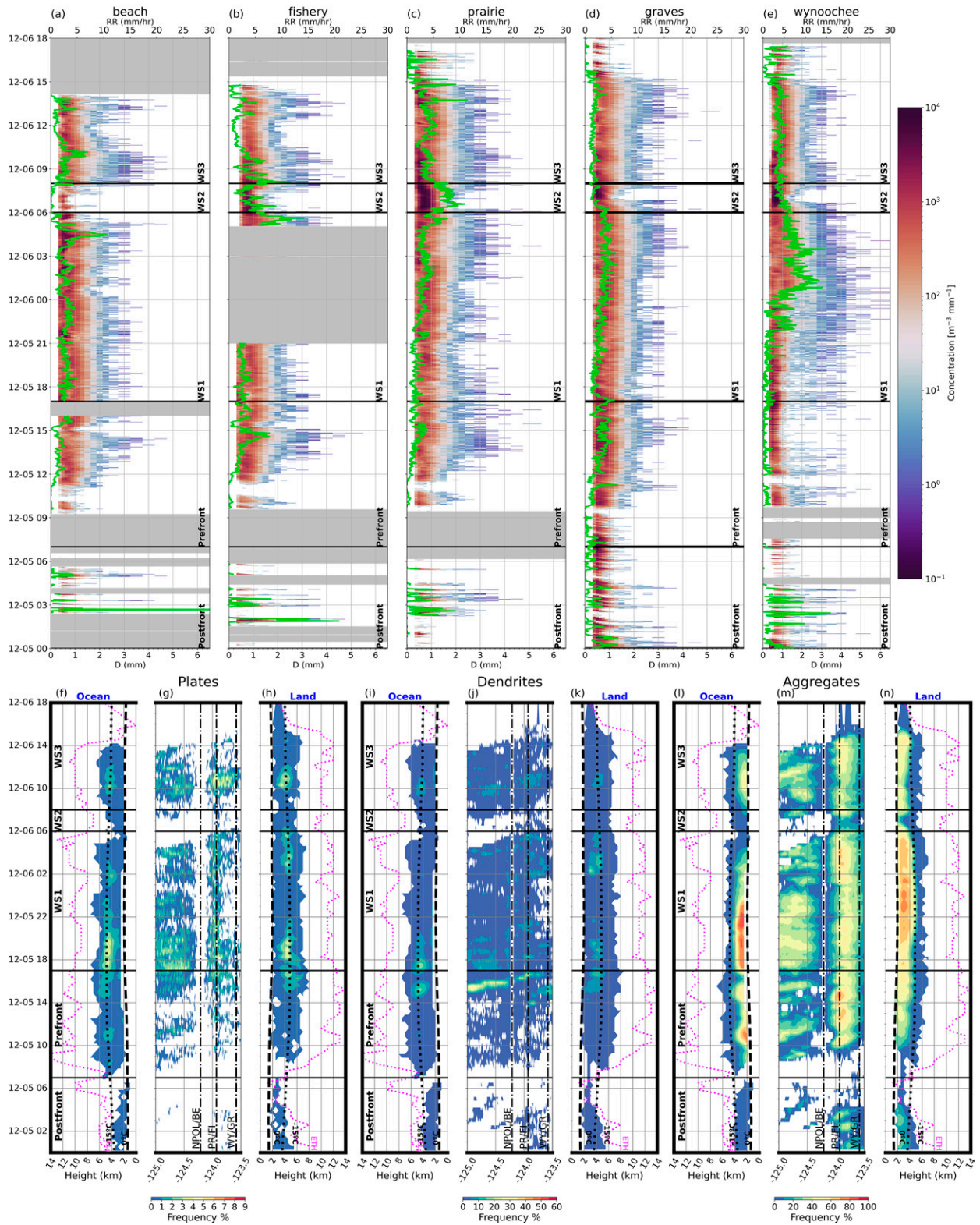
FIG. 13. As in Fig. 11, but for case 3, 5–6 Dec 2015.
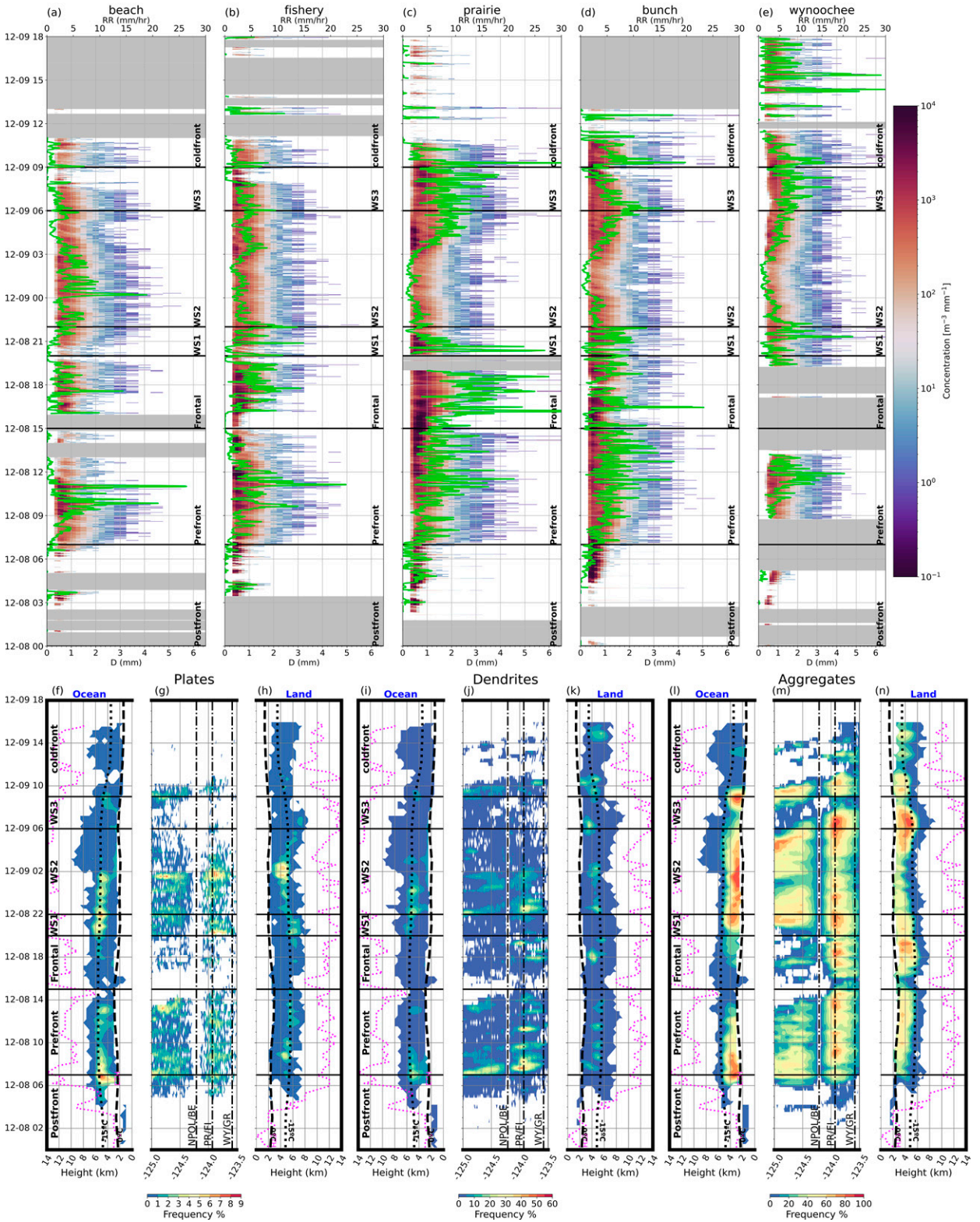
Case 4 Dec 08-09

FIG. 14. As in Fig. 11, but for case 4, 8–9 Dec 2015. In this case, Graves data was missing so Bunch is used as the inland site.

To summarize these findings, there is a clear preference for prolific dendritic concentrations around the $-10°$ to $-15°C$ height, and more frequent classifications of dendrites over the terrain compared to the ocean sector. This is consistent with the enhanced Z_{dr} layer that has been noted in this dataset (McMurdie et al. 2018; DeLaFrance et al. 2021), and is argued to enhance precipitation rates at the surface (Kennedy and Rutledge 2011; DeLaFrance et al. 2021). However, the Hovmöller analysis shows that dendritic layers can propagate from the ocean to the terrain. Nonetheless, there is a clear preference for enhanced DN and AG classifications at the longitude of the Prairie disdrometer, which is approximately located at the entrance to the Quinault Valley and the beginning of terrain higher than 500 m (Fig. 1). This could be an indicator of increased saturation levels as air is forced upward as it encounters the terrain, leading to further cooling. Aggregation of ice particles increases sizes, which then can survive longer in the melting layer (Thériault et al. 2006), and/or serve as "seeder drops" at the top of the warm layer that efficiently collect populous small drops as they fall. In all cases, higher frequencies of DN and AG were correlated with a broader DSD with larger maximum drop sizes at the disdrometer sites. However, this did not always result in higher rain rates. Particularly during the early periods of the warm sectors, higher rain rates were correlated with significant increases in the concentration of small drops (<1 mm) and seemed to have little impact from the changes to the bulk ice microphysics analyzed here, supporting the findings of Zagrodnik et al. (2018). Certain mesoscale periods were characterized by shallow ice cloud with low variability in large frozen particles (DN, PL, AG). These periods had high concentrations of very small drops (<1 mm) with a distinct lack of larger particles apparent in the disdrometer data (e.g., WS2 in case 2). And some periods, such as the WS3 and frontal, showed more surface DSD and rain rate response to the ice microphysics through increased sizes, as well as decreased concentrations of smaller drops.

c. Detailed radar studies of case 2 (17–18 November 2015)

We now contextualize the above analysis with specific high-resolution NPOL radar examples from case 2 (17–18 November AR) during different frontal regimes. A transect from over the ocean and through the Quinault Valley is constructed by taking the 236° and 54° radials (the latter being the azimuth to the Upper Quinault site) from NPOL; the scanning strategy was such that these are approximately 13 min apart in time. We note that the disdrometers did not fall directly along the 54° azimuth (see Table 2), but are placed for reference at their respective distances from NPOL for illustration purposes. The 1.5° elevation PPI is selected for the closest time after the land RHI (approximately 3 min later). Representative images from different time periods are shown, but loops of the entire periods can be found in the supplemental material.

As the warm front (WF) made landfall around 2300 UTC 16 November, the most striking feature is the sloped melting layer (ML) evidenced by the wet snow classification, reflectivity bright band (BB), and high Z_{dr} values (Figs. 15a–d). Over

the ocean the BB is relatively weak but stable around 2 km in height. Collision–coalescence signatures of increasing Z and Z_{dr} toward the surface (Kumjian and Prat 2014; Porcacchia et al. 2017) are evident at 40 km range over the ocean, demonstrating the role of warm rain processes in the deep warm layer in forming precipitation The radial velocity PPI indicates strong warm air advection with a low-level southerly jet turning to strong westerlies with height (Fig. 15m). A shallow surface layer of easterly flow is present immediately above the coastal terrain. The flow along the RHIs show a local elevated, sloping jet starting 50 km from NPOL over the ocean (Figs. 15g–h). The BB clearly slopes toward the terrain (Figs. 15b,d), leading to a local enhancement in surface Z_{dr} and Z values at the Prairie site (Figs. 15d,f). The sloping bright band could be the result of diabatic cooling due to melting snow, lowering the air temperature trapped against the terrain and effectively lowering the BB, as was observed in the Whistler valley (Thériault et al. 2015). It is also possible that environmental conditions such as the advection of low-θ_e air parallel to the terrain may contribute to cooling via evaporation as discussed by Minder and Kingsmill (2013). A shear layer between these two air masses is evidenced in the vertical radial velocity gradient and high SW from Prairie extending over the higher terrain, around 2 km MSL (Figs. 15h,j).

During WS1, the deep cold cloud (ETC up to 7 km MSL) and 2-km-deep warm cloud layer allowed for both ice and warm-rain processes to contribute to the surface DSDs (Fig. 16). The deep cold cloud exhibits clear dendritic growth just below the $-15°C$ isotherm (Figs. 16a,b), identified in the HCA as a layer of PL, indicative of planar crystals. Below this zone, aggregation dominates indicated by near-0 Z_{dr} values (Fig. 15f), increased reflectivity (Figs. 17c,d), and AG in the HCA (Figs. 17a,b). The BB is fairly thin, but moderately intense with reflectivities between 40 and 45 dBZ and Z_{dr} in the range of 2.5–3 dB. This is consistent with the melting of larger aggregates, which become wetted and highly reflective before fully collapsing to quasi-spherical drops. Interestingly, this signature is fairly uniform across the domain, although there is a slight reflectivity enhancement aloft beginning 20 km inland from NPOL at around 4 km MSL. Radial velocities show uniform west wind increasing in speed with height across the domain, with the exception of a shallow layer of down-valley flow to the ocean (Fig. 16h). There is an elevated shear layer over the ocean sector at around 3 km MSL (Fig. 16i), but the shear over the land associated with the low-level flow toward the radar under the deep westerlies weakened from the previous time (Figs. 16h,j).

The lack of large drops present in the DSDs during WS2 from 0600 to 0900 UTC 17 November (Figs. 12a–e) is associated with a synoptically weaker period with low precipitation rates and a lack of robust aggregation aloft (Fig. 17). ETHs were lower (generally 6 km MSL and below) and the overall echoes were weak (<30 dBZ, Figs. 17c,d,l). The cold cloud was primarily made up of IC, with a notable absence of a dendritic layer or an aggregation signature present, particularly over land (Figs. 17a,b,k). The upslope flow (Figs. 17g,h,m) lacked a strong up-valley jet that was present at other times (e.g., Fig. 15h), resulting in reduced super saturations with respect to ice aloft, and therefore less favorable conditions for
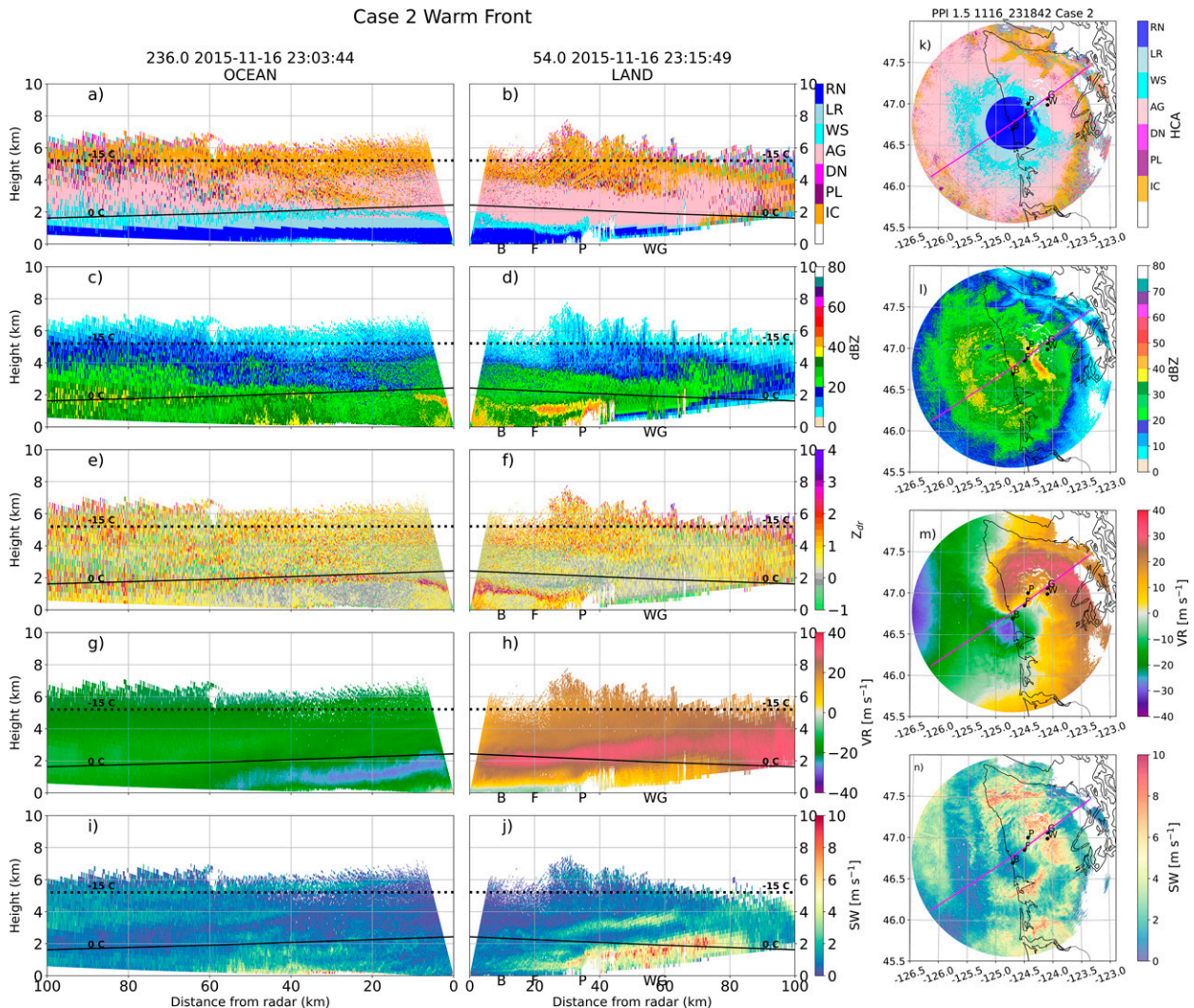
FIG. 15. RHI over the ocean (236°) and up the Quinault Valley (54°) during the Warm Front around 2300 UTC 16 Nov 2015. (a),(b) HCA; (c),(d) reflectivity; (e),(f) Z_{dr}; (g),(h) radial velocity; and (i),(j) spectrum width. PPIs at 1.5° at 2318 UTC (k) HCA, (l) reflectivity, (m) radial velocity, and (n) spectrum width. The −15°C (0°C) isotherms are indicated with dotted (solid) black lines on the RHIs, and the location of the RHIs is indicated on the PPIs with solid pink lines. The locations of the Beach, Fishery, Prairie, Wynoochee, and Graves disdrometers are represented in black letters.

dendritic growth. Thus, there were no large particles entering the warm layer, and the smaller drops at the surface were due to warm rain processes and melting of ice crystals, as indicated by the thin BB evident in Z_{dr} around 2 km MSL (Figs. 17e,f).

The WS3 period is characterized by deep cloud, with ETH up to 8 km (Figs. 18a–j). The echo over the ocean has nearly dissipated, and the precipitation is consolidated over the terrain (Figs. 18k–n). Interestingly, there is residual echo within 20 km of the coastline over the ocean (Fig. 18, ocean RHIs). There is a very clear dendritic layer in HCA around 6 km coinciding with the −15°C isotherm (Fig. 18b), identified by enhanced Z_{dr} values with moderate reflectivity over land (Figs. 18d,f). Below this layer is a robust aggregation signature with Z_{dr} values dropping to near 0 dB, and in this region the BB is thick and very evident (dBZ > 40 dBZ and Z_{dr} > 4 dB).

Below the BB the reflectivites and Z_{dr} remain high and exhibit a collision–coalescence signature, particularly over Fishery and Prairie. The big drops (larger than 2–4 mm) return at these sites, along with large concentrations of small drops, and the rain rates coincidently increase to >30 mm h^{-1} at Prairie (Fig. 12c). This period is also characterized by very strong upslope flow at all levels, with a westerly jet approaching 40 m s^{-1} below 2 km, directly up the Quinault Valley (Figs. 18g,h). We hypothesize that this low-level jet allowed for significant moistening leading to activation of numerous small drops in the warm layer, and created water saturated conditions aloft allowing dendritic growth. The aggregates, upon melting, readily collected small drops in this 2-km-deep warm layer. The strong uplift forced by the terrain provides a continuous supply of small drops, thereby resulting in high rain rates approaching
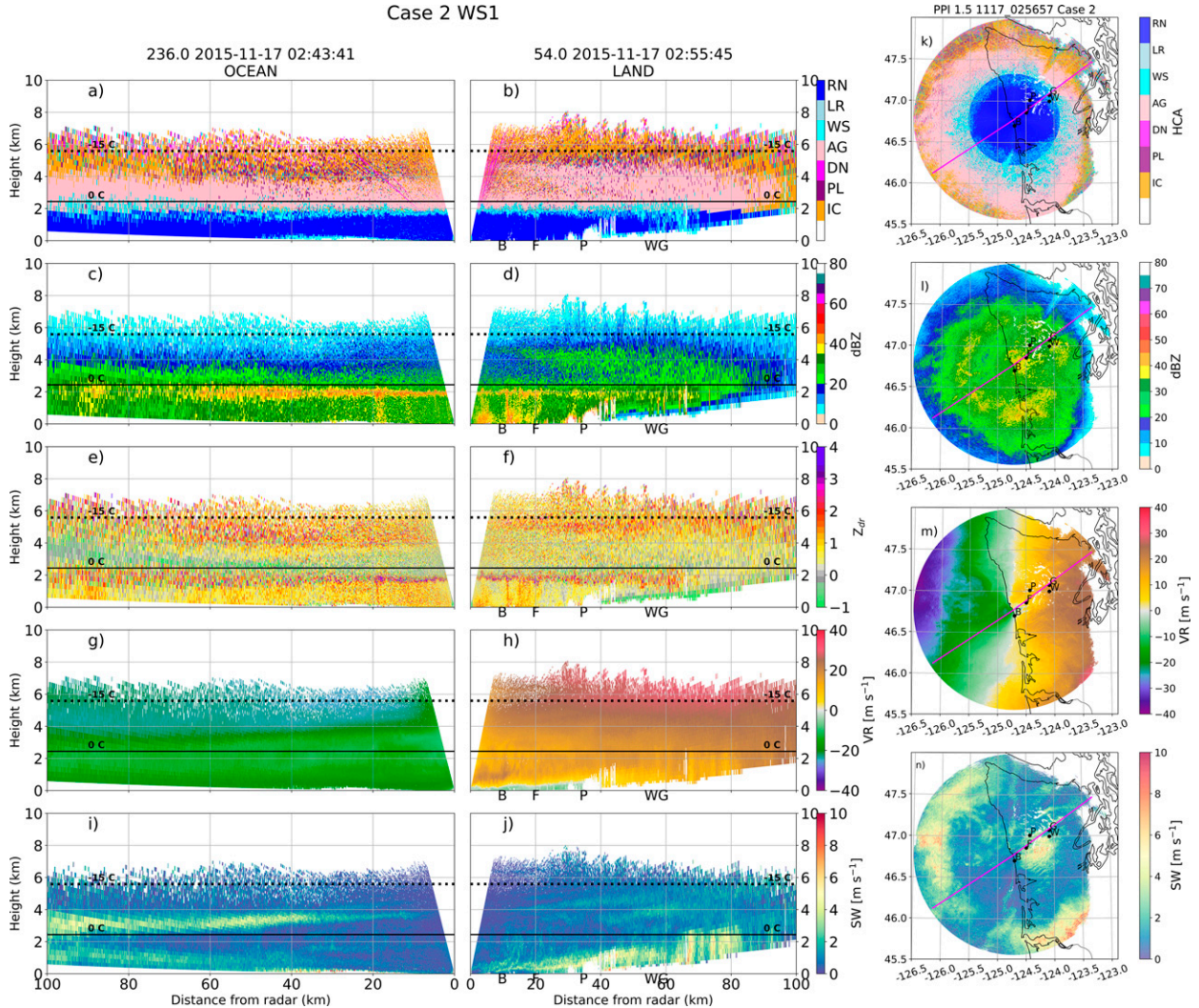
FIG. 16. As in Fig. 15, but during the first stage of the warm sector (WS1) around 0245 UTC.

30 mm h^{-1} due to the combined contributions of warm rain and ice-microphysical processes (Figs. 12c–e).

Finally, the NCFR moves through the domain from 2000 to 2300 UTC, ushering in a period of shallow convection and lower (1.6 km) ML (Fig. 19). This is evidenced over the ocean sector, with weak reflectivity turrets reaching only to 4 km in height (Fig. 19c). The land sector has deeper (up to 6 km), more uniform cold cloud above the ML (Fig. 19d), with some Z_{dr} enhancements along a shear boundary at 3 km, which suggest a region of larger particles through the DN classification (Figs. 19a–h). The layer of strong vertical speed shear at 2 km over the ocean intensifies as it impacts the terrain and rises to 3 km. This is characterized by the "braided" K–H signature in SW (Figs. 19i,j), and interestingly corresponds to a region of dendrites identified by the HCA, potentially associated with enhanced lifting and therefore locally enhanced water saturation. The NCFR is to the southeast of NPOL at this time, characterized by a wind shift in the radial velocity (Fig. 19m).

4. Conclusions and discussion

OLYMPEX provided a rich dataset for examining precipitation at many scales and across ocean through complex terrain surfaces. The ample rain sampled during the project allowed for analysis of several frontal systems as they made landfall and progressed over the complex terrain of the Olympic Mountains. Rainfall and bulk microphysics as a function of terrain height, synoptic regime, environment, and distance inland were analyzed. We found that all of these play a role in locally modifying the precipitation characteristics. Our findings support the conclusions of many previous studies, but provide a deeper look into the complex interplay between the microphysics, dynamics, and environment using polarimetric radar analysis compared with airborne in situ and ground-based disdrometer observations.

Analysis from the NPOL polarimetric S-band radar showed that up to 2000 mm of rain fell over the course of the radar
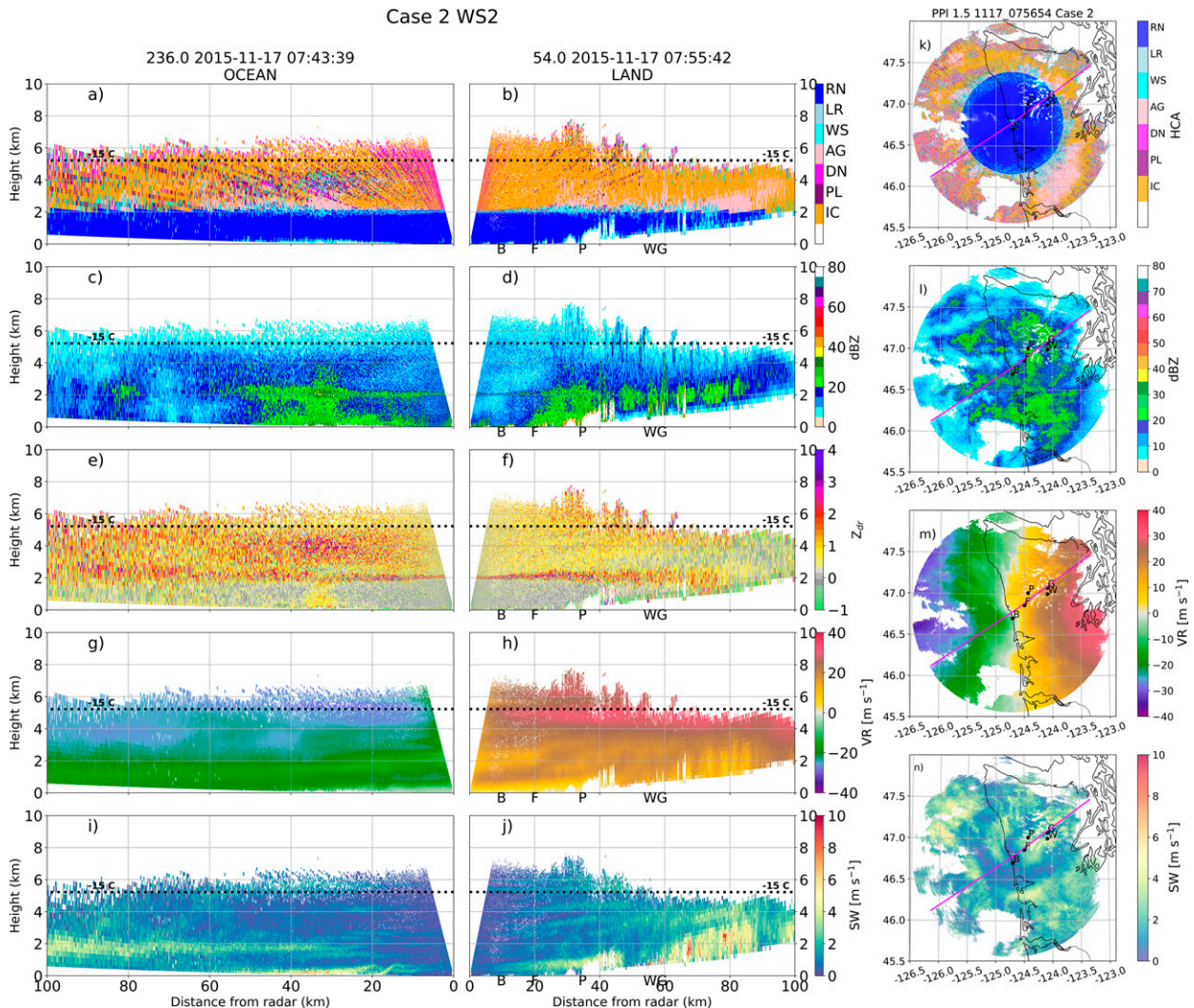
FIG. 17. As in Fig. 15, but during WS2, around 0745 UTC.

operations, with the most precipitation occurring over moderate terrain heights (100–1000 m) (Fig. 2). On many days, rainfall resulted in >50 mm day^{-1} km^{-2} in several terrain bands, with over 150 mm day^{-1} km^{-2} in the higher (>500 m) terrain bands during some cases (Fig. 3). We analyzed four cases in detail that exhibited notable orographic enhancement. All of the cases were associated with ARs, although three had wind patterns favorable for moisture transport directly up the Quinault Valley.

Early in the storm system evolution, during the prefrontal and warm sectors, rainfall coverage is widespread over the ocean and the terrain. As the warm sector pushed into the terrain, the mean rain rates increased over the terrain. Microphysical analysis using the NPOL polarimetric data revealed both deep warm and cold cloud structures, with frequent dendrite and plate-type crystals around the −10° to −15°C level, with prolific aggregation occurring below. Microphysical data from the Citation showed that many of the crystals in this layer had some branching structure or were rimed, which could allow for more favorable aggregation. During these times, larger raindrop sizes were present in the disdrometer observations, although often still coincident with significant concentrations of smaller drops. At times these larger drops were associated with a decrease in the small drop concentration, suggesting the larger aggregates were "seeding" the DSD below and readily colliding and coalescing with smaller drops as they fell to the surface. Several systems were characterized by distinct mesoscale periods, which had smaller rain rates and notable DSDs with large concentrations of drops smaller than 1 mm and a complete disappearance of larger drops (WS2). These periods had very little large ice aloft, but did have IC classifications, suggesting that perhaps small, compact crystals such as columns and bullet rosettes were melting and contributing to the concentration of small drops at the surface, but not significantly growing through collisions in the warm layer.

There was a clear preference for microphysical and dynamic enhancements at approximately 30 km inland from NPOL, which was the location of the Prairie disdrometer and the
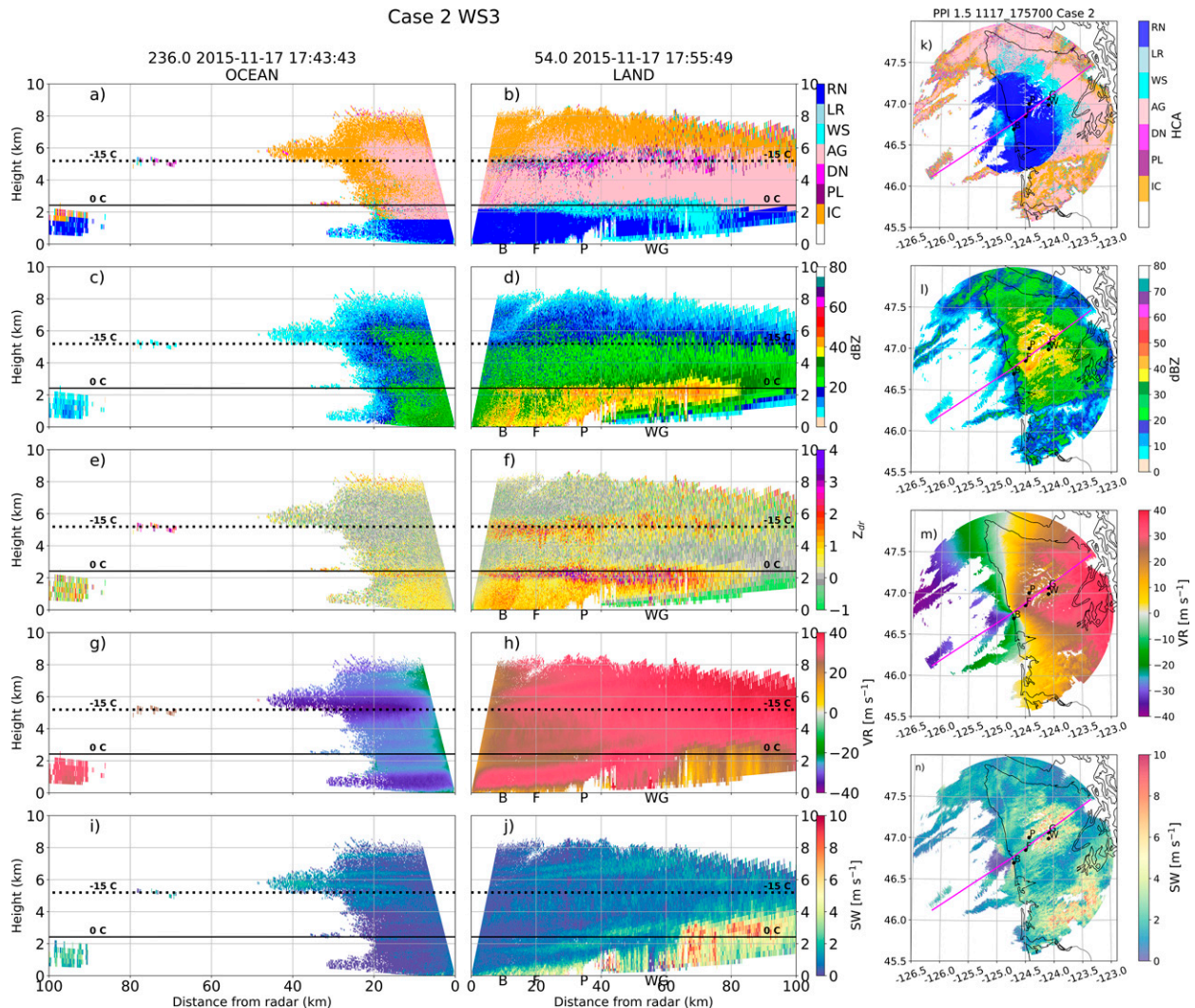
FIG. 18. As in Fig. 15, but during the WS3 period around 1745 UTC 17 Nov 2015.

approximate beginning of terrain with heights > 500 m. The DN and AG classifications were most frequent in this longitude band, and abrupt changes in the radar echo-top height were noted in the RHI analysis at this distance. Additionally, enhancements to spectrum width related to turbulence and shear flow were favorable. These mechanisms all, at times, may have played a role in the enhanced precipitation at Prairie and more generally in the middle terrain band (100–500 m).

While the DN layer was most often observed over the land, there were times showing propagation of dendritic layers from the ocean to the land, especially during the prefrontal periods just before the onset of the warm sector. Last, dynamics were important in creating small-scale waves such as Kelvin–Helmholtz waves and gravity waves along shear layers which locally enhanced lift and increased aggregation and/or collisions in the warm layer, increasing drop sizes. Larger flow patterns also played a role in the precipitation accumulations and microphysics. This was demonstrated in case 3, which had less favorable moisture transport directly into the terrain, but nonetheless had high

rainfall accumulations over the terrain. In this case, the strong southerly winds interacted with the terrain to create shear layers which locally enhanced aggregation. These had minor influences on the DSD characteristics but not necessarily on rainfall (also noted by Barnes et al. 2018).

We have further demonstrated the complexities of large synoptic systems impinging on the prominent terrain of the Olympic Peninsula. The surface precipitation is a complicated mix of ice and warm-rain processes, locally enhanced by interactions between the large-scale environment, mesoscale features, and the terrain. Features in the ice cloud, such as layers of dendrites and plates, play a role in modulating the surface DSD by increasing the drop sizes (via melting), although during times of significant IVT and deep warm layers, the impact on surface precipitation is small compared to the prolific warm-rain processes. At other times, these larger "seed" drops readily collected smaller drops in the warm cloud zone modifying the surface DSD by shifting the distribution toward larger drops. Also, during times with very small crystals aloft, there is
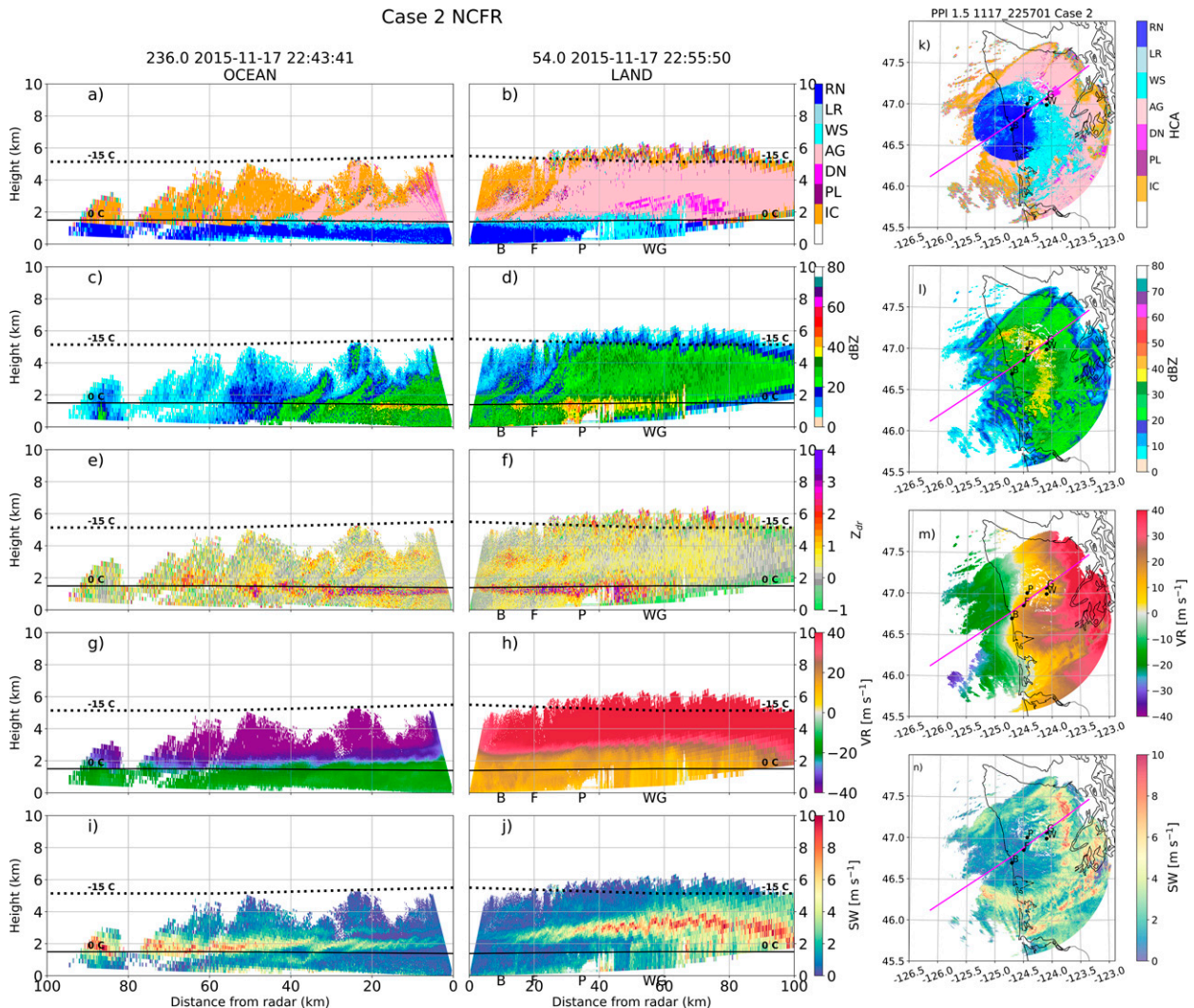
FIG. 19. As in Fig. 15, but during the passage of the NCFR around 2245 UTC 17 Nov 2015.

a notable lack of larger rain drops below. Characterizing these complex interactions demonstrates the continuing challenge of estimating precipitation in this tricky environment, but is critical for understanding and improving satellite precipitation retrievals.

and rain-rate algorithms were applied using CSU_Radartools open software (https://github.com/CSU-Radarmet/CSU_Radar Tools). MERRA2 data were downloaded from NASA's Global Modeling and Assimilation Office.

REFERENCES

Barnes, H. C., J. P. Zagrodnik, L. A. McMurdie, A. K. Rowe, and R. A. Houze Jr., 2018: Kelvin–Helmholtz waves in precipitating midlatitude cyclones. *J. Atmos. Sci.*, **75**, 2763–2785, https://doi.org/10.1175/JAS-D-17-0365.1.

Brandes, E. A., G. Zhang, and J. Vivekanandan, 2002: Experiments in rainfall estimation with a polarimetric radar in a subtropical environment. *J. Appl. Meteor.*, **41**, 674–685, https://doi.org/10.1175/1520-0450(2002)041<0674:EIREWA> 2.0.CO;2; Corrigendum, **44**, 186, https://doi.org/10.1175/1520-0450(2005)44<186:C>2.0.CO;2.

Chen, H., V. Chandrasekar, and R. Bechini, 2017: An improved dual-polarization radar rainfall algorithm (DROPS2.0):

Application in NASA IFloodS field campaign. *J. Hydrometeor.*, **18**, 917–937, https://doi.org/10.1175/JHM-D-16-0124.1.

Cifelli, R., V. Chandrasekar, S. Lim, P. C. Kennedy, Y. Wang, and S. A. Rutledge, 2011: A new dual-polarization radar rainfall algorithm: Application in Colorado precipitation events. *J. Atmos. Oceanic Technol.*, **28**, 352–364, https://doi.org/10.1175/2010JTECHA1488.1.

Conrick, R., and C. F. Mass, 2019: An evaluation of simulated precipitation characteristics during OLYMPEX. *J. Hydrometeor.*, **20**, 1147–1164, https://doi.org/10.1175/JHM-D-18-0144.1.

DeLaFrance, A., L. McMurdie, and A. Rowe, 2021: Orographically modified ice-phase precipitation processes during the Olympic Mountains Experiment (OLYMPEX). *J. Atmos. Sci.*, **78**, 3815–3833, https://doi.org/10.1175/JAS-D-21-0091.1.

Delene, D., 2017: GPM ground validation UND citation navigation data OLYMPEX V1. NASA EOSDIS Global Hydrology Resource Center Distributed Active Archive Center, accessed 30 March 2021, https://doi.org/10.5067/GPMGV/OLYMPEX/NAV/DATA101.

Doviak, R. J., and D. S. Zrnić, 2006: *Doppler Radar and Weather Observations.* 2nd ed. Dover Publications, 592 pp.

Friedrich, K., S. Higgins, F. J. Masters, and C. R. Lopez, 2013: Articulating and stationary PARSIVEL disdrometer measurements in conditions with strong winds and heavy rainfall. *J. Atmos. Oceanic Technol.*, **30**, 2063–2080, https://doi.org/10.1175/JTECH-D-12-00254.1.

Gao, Y., J. Lu, L. R. Leung, Q. Yang, S. Hagos, and Y. Qian, 2015: Dynamical and thermodynamical modulations on future changes of landfalling atmospheric rivers over western North America. *Geophys. Res. Lett.*, **42**, 7179–7186, https://doi.org/10.1002/2015GL065435.

Giangrande, S. E., J. M. Krause, and A. V. Ryzhkov, 2008: Automatic designation of the melting layer with a polarimetric prototype of the WSR-88D radar. *J. Appl. Meteor. Climatol.*, **47**, 1354–1364, https://doi.org/10.1175/2007JAMC1634.1.

Heymsfield, A., A. Bansemer, and M. Poellot, 2017: GPM ground validation NCAR particle probes OLYMPEX V1. NASA EOSDIS Global Hydrology Resource Center Distributed Active Archive Center, accessed 31 March 2021, https://doi.org/10.5067/GPMGV/OLYMPEX/PROBES/DATA201.

Houze, R. A., Jr., and S. Medina, 2005: Turbulence as a mechanism for orographic precipitation enhancement. *J. Atmos. Sci.*, **62**, 3599–3623, https://doi.org/10.1175/JAS3555.1.

——, and Coauthors, 2017: The Olympic Mountains Experiment (OLYMPEX). *Bull. Amer. Meteor. Soc.*, **98**, 2167–2188, https://doi.org/10.1175/BAMS-D-16-0182.1.

Jackson, R., and Coauthors, 2021: The applicability of specific attenuation based rainfall rate retrievals in the tropics. *Atmos. Meas. Tech.*, **14**, 53–69, https://doi.org/10.5194/amt-14-53-2021.

Kennedy, P. C., and S. A. Rutledge, 2011: S-band dual-polarization radar observations of winter storms. *J. Appl. Meteor. Climatol.*, **50**, 844–858, https://doi.org/10.1175/2010JAMC2558.1.

Kumjian, M. R., and O. Prat, 2014: The impact of raindrop collisional processes on the polarimetric radar variables. *J. Atmos. Sci.*, **71**, 3052–3067, https://doi.org/10.1175/JAS-D-13-0357.1.

Lang, T. J., S. W. Nesbitt, and L. D. Carey, 2009: On the correction of partial beam blockage in polarimetric radar data. *J. Atmos. Oceanic Technol.*, **26**, 943–957, https://doi.org/10.1175/2008JTECHA1133.1.

Mass, C. F., and G. K. Ferber, 1990: Surface pressure perturbations produced by an isolated mesoscale topographic barrier. Part I: General characteristics and dynamics. *Mon. Wea. Rev.*, **118**, 2579–2596, https://doi.org/10.1175/1520-0493(1990)118<2579:SPPPBA>2.0.CO;2.

McMurdie, L. A., A. K. Rowe, R. A. Houze Jr., S. R. Brodzik, J. P. Zagrodnik, and T. M. Schuldt, 2018: Terrain-enhanced precipitation processes above the melting layer: Results from OLYMPEX. *J. Geophys. Res. Atmos.*, **123**, 12–194, https://doi.org/10.1029/2018JD029161.

Minder, J. R., and D. E. Kingsmill, 2013: Mesoscale variations of the atmospheric snow line over the northern Sierra Nevada: Multiyear statistics, case study, and mechanisms. *J. Atmos. Sci.*, **70**, 916–938, https://doi.org/10.1175/JAS-D-12-0194.1.

Naeger, A. R., B. A. Colle, N. Zhou, and A. Molthan, 2020: Evaluating warm and cold rain processes in cloud microphysical schemes using OLYMPEX field measurements. *Mon. Wea. Rev.*, **148**, 2163–2190, https://doi.org/10.1175/MWR-D-19-0092.1.

Parsons, D. B., and P. V. Hobbs, 1983: The mesoscale and microscale structure and organization of clouds and precipitation in midlatitude cyclones. XI: Comparisons between observational and theoretical aspects of rainbands. *J. Atmos. Sci.*, **40**, 2377–2398, https://doi.org/10.1175/1520-0469(1983)040<2377:TMAMSA>2.0.CO;2.

Petersen, W. A., A. Tokay, P. N Gatlin, and M. T. Wingo, 2017: GPM Ground Validation Autonomous Parsivel Unit (APU) OLYMPEX V1. NASA Global Hydrometeorology Resource Center DAAC, accessed 13 June 2016, https://doi.org/10.5067/GPMGV/OLYMPEX/APU/DATA301.

Poellot, M. R., A. Heymsfield, and A. Bansemer, 2017: GPM ground validation UND citation cloud microphysics OLYMPEX V1. NASA EOSDIS Global Hydrology Resource Center Distributed Active Archive Center, accessed 5 March 2021, https://doi.org/10.5067/GPMGV/OLYMPEX/MULTIPLE/DATA201.

Porcacchia, L., P. E. Kirstetter, J. J. Gourley, V. Maggioni, B. L. Cheong, and M. N. Anagnostou, 2017: Toward a polarimetric radar classification scheme for coalescence-dominant precipitation: Application to complex terrain. *J. Hydrometeor.*, **18**, 3199–3215, https://doi.org/10.1175/JHM-D-17-0016.1.

Pruppacher, H. R., and J. D. Klett, 1997: *Microphysics of Clouds and Precipitation.* 2nd ed. Kluwer Academic Publishers, 954 pp.

Purnell, D. J., and D. J. Kirshbaum, 2018: Synoptic control over orographic precipitation distributions during the Olympics Mountains Experiment (OLYMPEX). *Mon. Wea. Rev.*, **146**, 1023–1044, https://doi.org/10.1175/MWR-D-17-0267.1.

Rutledge, S. A., V. Chandrasekar, B. Fuchs, J. George, F. Junyent, B. Dolan, P. C. Kennedy, and K. Drushka, 2019: SEA-POL goes to sea. *Bull. Amer. Meteor. Soc.*, **100**, 2285–2301, https://doi.org/10.1175/BAMS-D-18-0233.1.

Siler, N., G. Roe, and D. Durran, 2013: On the dynamical causes of variability in the rain-shadow effect: A case study of the Washington Cascades. *J. Hydrometeor.*, **14**, 122–139, https://doi.org/10.1175/JHM-D-12-045.1.

Thériault, J. M., R. E. Stewart, J. A. Milbrandt, and M. K. Yau, 2006: On the simulation of winter precipitation types. *J. Geophys. Res.*, **111**, D18202, https://doi.org/10.1029/2005JD006665.

——, J. A. Milbrandt, J. Doyle, J. R. Minder, G. Thompson, N. Sarkadi, and I. Geresdi, 2015: Impact of melting snow on the valley flow field and precipitation phase transition. *Atmos. Res.*, **156**, 111–124, https://doi.org/10.1016/j.atmosres.2014.12.006.

Thompson, E. J., S. A. Rutledge, B. Dolan, V. Chandrasekar, and B. L. Cheong, 2014: Development of a polarimetric radar hydrometeor classification algorithm for winter precipitation.

J. Atmos. Oceanic Technol., **31**, 1457–1481, https://doi.org/10.1175/JTECH-D-13-00119.1.

Ulbrich, C. W., 1983: Natural variations in the analytical form of the raindrop size distribution. *J. Climate Appl. Meteor.*, **22**, 1764–1775, https://doi.org/10.1175/1520-0450(1983)022<1764:NVITAF>2.0.CO;2.

Willis, P. T., 1984: Functional fits to some observed drop size distributions and parameterization of rain. *J. Atmos. Sci.*, **41**, 1648–1661, https://doi.org/10.1175/1520-0469(1984)041<1648:FFTSOD>2.0.CO;2.

Wolff, D., D. Marks, W. A. Petersen, and J. Pippitt, 2017: GPM ground validation NASA S-band dual polarimetric (NPOL) Doppler radar OLYMPEX V2. NASA EOSDIS Global Hydrology Resource Center Distributed Active Archive Center, accessed 8 November 2016, https://doi.org/10.5067/GPMGV/OLYMPEX/NPOL/DATA301.

Zagrodnik, J. P., L. A. McMurdie, and R. A. Houze Jr., 2018: Stratiform precipitation processes in cyclones passing over a coastal mountain range. *J. Atmos. Sci.*, **75**, 983–1004, https://doi.org/10.1175/JAS-D-17-0168.1.

——, L. McMuride, and R. Conrick, 2021: Microphysical enhancement processes within stratiform precipitation on the barrier and sub-barrier scale of the Olympic Mountains. *Mon. Wea. Rev.*, **149**, 503–520, https://doi.org/10.1175/MWR-D-20-0164.1.